Universidade de Lisboa
Faculdade de Ciências
Departamento de Física

Anatomical glenoid replacement: a homogenized and micro-finite element analysis

Inês Isabel Gonçalves Santos

Dissertação
Mestrado Integrado em Engenharia Biomédica e Biofísica
Perfil de Engenharia Clínica e Instrumentação Médica

2014

Universidade de Lisboa
Faculdade de Ciências
Departamento de Física

Anatomical glenoid replacement: a homogenized and micro-finite element analysis

Inês Isabel Gonçalves Santos

Dissertação orientada por:
Dr. Yan Chevalier
Professor Ricardo Salvador

Mestrado Integrado em Engenharia Biomédica e Biofísica
Perfil de Engenharia Clínica e Instrumentação Médica

2014

Sim, sei bem
Que nunca serei alguém.
Sei de sobra
Que nunca terei uma obra.
Sei enfim,
Que nunca saberei de mim.
Sim, mas agora,
Enquanto dura esta hora,
Este luar, estes ramos,
Esta paz em que estamos,
Deixem-me crer
O que nunca poderei ser.

Ricardo Reis, in *"Odes"*

Acknowledgments

I would like to express my deepest gratitude and appreciation to Dr. Yan Chevalier for giving me this opportunity to work under his supervision and grow as a research scientist. I would also like to thank him for all the guidance, expertise and patience that were keystones in the accomplishment of this thesis.

I am also grateful to Dr. Matthias Pietschmann, from the Klinikum Grosshadern, for his insight and help with dissecting the specimens. It was one of the coolest things I have ever done.

I thank Professor Ricardo Salvador, my supervisor in Portugal, for all the advice and for introducing me to the micro finite element analysis.

I would like to thank all my colleagues from the laboratory for welcoming me and helping me with the German language. A special thank you to Theresa and Julia, for the daily lunches, the happy moments and the troubled days that we shared.

I must also acknowledge the Faculdade de Ciências da Universidade de Lisboa and my professors, for these five years of instruction and knowledge, without which I would not have come this far.

Um agradecimento muito especial aos meu pais, Maria Antónia Gonçalves e Manuel Santos, pelo seu apoio, amor e dedicação. Quero agradecer à minha avó, Rosa Carloto, por me incentivar sempre a estudar e ir mais longe, e à minha avó, Maria Tomásia Gonçalves, por se preocupar sempre tanto comigo. Um grande obrigado também à minha prima e amiga Marisa Caixas, por ser um exemplo de força e determinação para mim. Espero deixá-los a todos orgulhosos.

Agradeço também a todos os meus amigos que, apesar da distância e desencontros, sabem sempre receber-me de braços abertos.

Finalmente, quero agradecer ao Tiago Marcelos, pelo amor e apoio incondicional.

Abstract

Despite the great improvements of Total Shoulder Arthroplasty (TSA) over the last few years, after surgery complications, such as glenoid loosening, continue to arise in some patients. Bone quality, glenohumeral conformity, cementing techniques, orientation or implant design are factors that affect the fixation of the glenoid component, therefore leading to loosening. Finite element (FE) analysis has been used to evaluate the effects of implant-related factors on the risks of fracture and loosening using simplified classical homogenized models without geometrical and material distinction between the cortical and cancellous bone. It was shown that more refined models give better insights into internal load sharing and risks of fracture, as well as trabecular orientation has a significant effect in the stiffness and strength of cancellous bone.

Therefore, this thesis aimed at using a combination of classical and refined micro-FE modelling of the implanted shoulder to evaluate different implantation scenarios, with emphasis at the load distribution and risks of loosening of the glenoid component. The effects of glenoid anatomic correction, different implant designs, loading conditions and cementing techniques were tested.

The results suggest that the keeled implant design provides a better stress distribution, spreading the compressive load away from the glenoid surface, thus sparing more cancellous bone. The introduction of a cement layer provides better fixation, however increases stress around the implant. Although both FE approaches yielded similar results, the micro-FE approach revealed more accurately how internal bone tissue is affected by design and loading conditions, which can be useful in understanding the bone remodelling mechanism.

Key-words: total shoulder arthroplasty, glenoid component, glenoid loosening, micro-finite element modelling, keeled and pegged designs

Sumário

Apesar das grandes melhorias que ocorreram na artroplastia total do ombro ao longo dos últimos anos, complicações pós-cirurgicas, como o afrouxamento do componente glenoidal, continuam a surgir em alguns pacientes. A qualidade óssea, a conformidade glenoumeral, as técnicas de cimentação, a orientação ou o design do implante são fatores que afetam a fixação do componente glenoidal, levando ao afrouxamento da mesmo. A análise de elementos finitos tem sido utilizada para avaliar os efeitos de fatores relacionados com o implante sobre os riscos de fratura e afrouxamento, usando modelos clássicos homogeneizados e simplificados, sem distinção geométrica e material entre o osso cortical e esponjoso. Observou-se em estudos anteriores que modelos representativos da escápula mais refinados fornecem uma melhor compreensão acerca da distribuição de cargas internamente e os riscos de fratura, bem como a orientação trabecular tem um efeito significativo na rigidez e resistência do osso esponjoso.

Esta dissertação teve como objetivo utilizar uma combinação do modelo clássico de método de elementos finitos com o método de elementos micro-finitos para avaliar diferentes cenários de implantação de próstes no ombro, com ênfase na distribuição de carga e os riscos de afrouxamento do componente glenoidal. Foram estudados os efeitos da correcção anatómica do glenóide, de diferentes designs do implante, condições de carga e técnicas de cimentação.

Os resultados sugerem que o design de quilha proporciona uma melhor distribuição de tensões, espalhando a força compressiva mais longe da superfície glenoidal e poupando, assim, mais o osso esponjoso. A introdução de uma camada de cimento proporciona uma melhor fixação, no entanto, aumenta a tensão em torno do implante. Embora se tenham obtido resultados semelhantes com ambas as abordagens de método de elementos finitos, a abordagem de elementos micro-finitos revelou com mais precisão como o tecido ósseo interno é afetado pelo design do implante e a forma como é aplicada a força, o que pode ser útil na compreensão do mecanismo de remodelação óssea.

Palavras-chave: artroplastia total do ombro, componente glenoidal, afrouxamento glenoidal, modelo de elementos micro-finitos, design de quilha e cavilha

Contents

List of Figures

List of Tables

List of Acronyms

AP Anterior-Posterior

BMD Bone Mass Density

BV Bone Volume

BV/TV Bone Volume Fraction

CAD Computer Aided Design

CT Computed Tomography

FE Finite element

HR-pQCT High-Resolution Peripheral QCT

LMU Ludwig-Maximilians Universität München

LVDT Linear Variable Differential Transformer

MIL Mean Intercept Length

MRI Magnetic Ressonance Imaging

QCT Quantitative Computed Tomography

PMMA Polymethylmethacrylate

PVC Polyvinyl Chloride

RVE Representative Volume Element

SI Superior-Inferior

STL STereoLithography

TSA Total Shoulder Arthroplasty

VTK Visualization Toolkit

Chapter 1

Introduction

1.1 Motivation

Shoulder arthroplasty has improved tremendously over the last few years. Total and reverse shoulder arthroplasty are, nowadays, generally successful procedures to treat patients with problems such as upper humerus fractures, painful and disabling shoulder joints due to osteoarthritis, inflammatory rheumatoid arthritis or severe rotator cuff tear. However, some complications may still occur after surgery: aseptic loosening of the implant, instability, infection and bone fractures may arise in some patients. Nowadays, despite of the improvements in this area, the risk factors, the treatment, the influence of prosthetic design and the ultimate fate of the implant are elements that remain weakly understood (Chalmers et al., April 2004).

The most frequent complication after shoulder arthroplasty is glenoid loosening. Some studies (Zhang et al., Mar 2013; Suárez, Nerkens, Valstar, Rozing, & van Keulen, Apr 2012) suggest that the occurrence of loosening could be related not only to patient-specific factors, like bone quality, but also to biomechanical factors related to implant features that affect fixation of the glenoid component. These factors refer to glenohumeral conformity, cementing techniques, orientation or design.

FE analysis has been used to evaluate the effects of implant-related factors on the risk of fracture and loosening in a standardized way, and also predict how typical biomechanical

loads are transmitted across the joint and how these are sustained at the cemented or cementless bone-implant interface (Gupta, van der Helm, & van Keulen, 2004; Terrier, Büchler, & Farron, 2005). For this, Gupta et al used models created with heterogeneous bone properties scaled with Quantitative Computed Tomography (QCT)-based bone mineral density and suggested that a part of the subchondral bone along the longitudinal axis of the glenoid cavity should be preserved to strengthen the glenoid structure and reduce the use of cement.

While most authors have used simplified classical homogenized models with isotropic material properties for bone without geometrical and material distinction between the cortical and cancellous bone region (Gupta et al., 2004; Terrier et al., 2005; Zhang et al., Mar 2013), a recent study (Yongpravat et al., 2013) demonstrated that the effects of the orientation of the glenoid component are affected by the model description, in particular how bone structures are modelled. This showed that more refined models with cortical and trabecular bone give better insights into the biomechanical response to applied loads.

Recent developments in numerical bone analysis coupled with high-resolution imaging have allowed the use of micro finite element analysis in the evaluation of structural behaviour of partial and whole bones (Pahr, Dall'Ara, Varga, & Zysset, 2012; Chevalier, Pahr, Allmer, Charlebois, & Zysset, 2007). These methods allow obtaining predictions of mechanical stiffness that are surpassing most of the classical homogenized finite element approaches.

While such methods have been used to investigate the effects of fracture repair at the spine (Kosmopoulos & Keller, Nov 2004), so far no study on the prosthetized glenoid has included a refined representation of bone structures. Such an approach would be useful to evaluate more accurately how internal bone tissue is affected by design changes in the prosthetized shoulder. In particular, a better modelling of bone structures that include the effects of trabecular network might reveal more accurately how changes in design at the glenoid can influence bone stresses and how these could lead to bone remodelling and potential loosening of the implant. Similar methods may be used to evaluate how design changes can modify the fixation stiffness of glenoid components and how this is affected by bone quality and implant positioning.

1.2 Objectives

The main objective of this thesis was to develop a reliable methodology, using a combination of classical FE and refined micro-FE modelling, to investigate on the fixation stability and load distribution of surgical replacement of the glenoid at the shoulder joint. More specifically, to investigate how internal loads in the bone are affected by different implantation scenarios regarding the design of the implant, loading conditions and cementing techniques. For this personalized models of the augmented glenoid were created from implant computed assisted drawings geometry and high-resolution medical images. This was accomplished through the following steps:

1. Preparation and scanning of the specimens of the shoulder joint that will be used in the validation of the numerical models;

2. Virtual implantation of two prosthetized glenoid components (keeled and pegged) using the Computer Aided Design (CAD) data and a high-resolution image of the scapula, positioned according to the surgical guidelines of the manufactures;

3. Development of a classical FE model by meshing the bone image and the superimposed glenoid components geometry and assigning nonlinear material properties based on existing material models and data from high-resolution images of the bone. Material properties were taken from the available literature related to the glenoid components;

4. Development of a micro-FE model by converting the resulting voxel image from the virtual implantation using custom made computer scripts developed at the lab following an established methodology;

5. Assignment of boundary conditions based on the positions of the soft tissue insertions mapped on the high-resolution image and definition of different load cases;

6. Static finite element analyses using a commercial software (ABAQUS, Simulia) for the classical FE model, to allow the investigation of fixation strength of the glenoid compo-

nents. The micro-FE model was solved using a dedicated open-source parallel solver (parFE, ETHZ), to obtain stresses in the bone elements and compare different loading scenarios and bone-implant configurations.

Material criteria based on literature were used to quantify local bone tissue damage and onset of bone remodelling. The density of bone tissue exceeding these criteria was computed, providing an objective mean to compare the effects of the different modelled configurations.

1.3 Outline of the thesis

My internship took place at the Labor für Biomechanik und Experimentalle Orthopädie of the Klinikum Grosshadern, Ludwig-Maximilians Universität München (LMU), from February to September 2014, under the supervision of Dr. Yan Chevalier (LMU) and Prof. Ricardo Salvador (FCUL) and co-supervision of Dr. med. Matthias Pietschmann (orthopedic surgeon of the affiliated hospital, Klinikum Grosshadern).

This thesis reflects my work during the internship and it is divided into seven chapters. **Chapter one** introduces the main after surgery complications that may arise from total shoulder arthroplasty followed by an overview of the outcomes of previous studies and the numerical methods that can provide a better understanding of the bone-implant system.

In **Chapter two** the background regarding these thesis is presented, introducing the anatomical, biomechanical and numerical considerations used in the study of glenoid replacement in the shoulder joint. The concepts of bone mechanics, shoulder's anatomy, finite element analysis and imagiology techniques used in this project are explained.

Chapter tree deals with the state-of-the-art of this thesis and presents the procedure behind total shoulder arthroplasty, clarifying important biomechanical and surgical concepts. The main complications of the procedure, such as the risk of glenoid loosening are also presented.

In **Chapter four** the materials and methodologies used in this thesis are presented. The results obtained are presented in **Chapter five** and their analysis and discussion is given in

Chapter six. Finally, the conclusions are presented in **Chapter seven**.

Chapter 2

Background

The mechanical behaviour of the shoulder joint depends on its structural configuration and bone properties. This chapter presents the anatomical and biomechanical background considered relevant to investigate on the fixation stability and load distribution of surgical replacement of the glenoid at the shoulder joint. Important fundamental concepts of finite element analysis, in the context of the commercial tools used, and imaging techniques that contribute to improve the results accuracy, in this and previous studies, are also mentioned.

2.1 Anatomy of the shoulder joint

The shoulder joint, also referred to as glenohumeral joint, is composed of tree bones: humerus (upper arm bone), scapula (shoulder blade) and clavicle (collarbone) as well as associated muscles, ligaments and tendons.

The scapula is a flat, triangular bone with the apex (the inferior angle) directed inferiorly (Figure 2.1). The large acromion process of the scapula has tree functions: to form a protective cover for the shoulder joint, to form the attachment site for the clavicle and to provide attachment points for some of the shoulder muscles. The smaller caracoid process provides attachments for some shoulder and arm muscles. A glenoid cavity, located in the superior lateral portion of the bone, articulates with the head of the humerus.

The glenohumeral joint is a ball-and-socket joint in which stability is reduced and mobility is increased compared to the hip joint (another ball-and-socket joint). Flexion, extension,

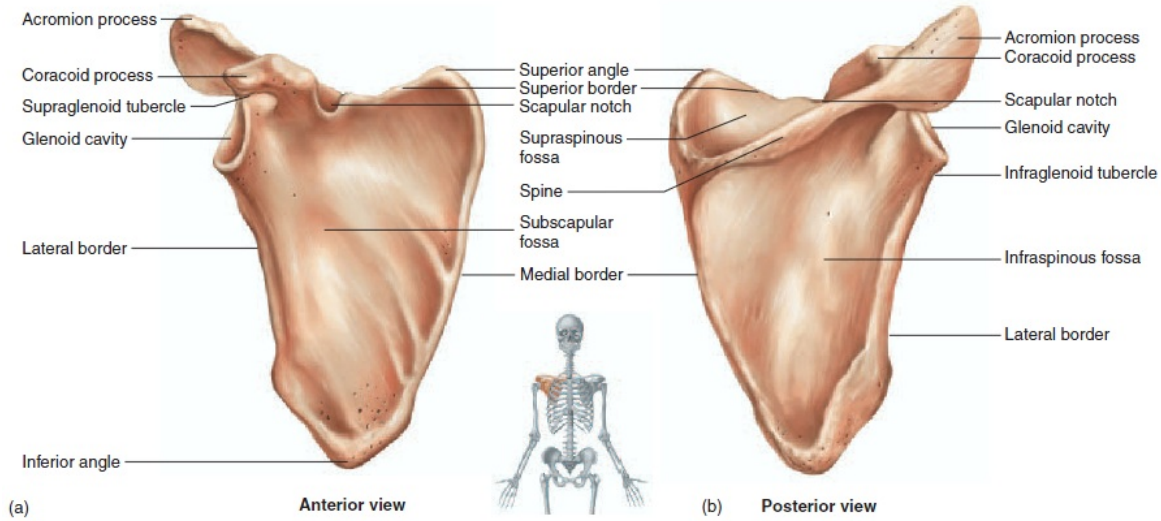

Figure 2.1: Right scapula: anterior and posterior views (Seeley et al., 2007).

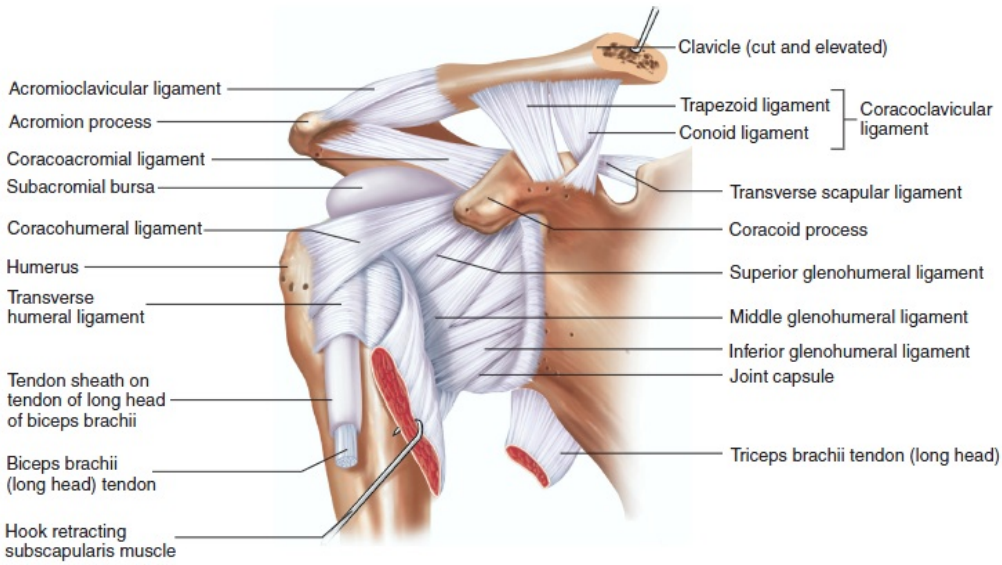

Figure 2.2: Anterior view of the right glenohumeral joint: tendons and ligaments (Seeley et al., 2007).

abduction, adduction, rotation and circumduction can all occur at the shoulder joint. The rounded head of the humerus articulates with the shallow glenoid cavity of the scapula. The rim of the glenoid cavity is built up slightly by a fibrocartilage ring, the glenoid labrum, to which the joint capsule is attached. A subscapular and subacromial bursa open into the

joint cavity (Figure 2.2).

The stability of the joint is maintained primarily by tree sets of ligaments and four muscles. The ligaments are the glenohumeral (superior, middle and inferior) ligament, the transverse humeral ligament, the coracohumeral ligament, which crosses from the root of the coracoid process to the humeral neck, and the coracoacromial ligament, which crosses above the joint between the coracoid process and the acromion process, being an accessory ligament. The glenohumeral ligament consists of tree slightly thickened longitudinal sets of fibers on the anterior side of the capsule that extend from the humerus to the margin of the glenoid cavity. The transverse humeral consists of lateral, transverse fibrous thickening of the joint capsule and crosses between the greater and lesser tubercles, holding down the tendon from the long head of the biceps muscle.

The four muscles, referred to collectively as the rotator cuff, pull the humeral head superiorly and medially toward the glenoid cavity. The head of the humerus is also supported against the glenoid cavity by the tendon from the biceps brachii muscle in the anterior part of the arm. This tendon is unusual in that it passes through the articular capsule of the shoulder joint before crossing the head of the humerus and attaching to the scapula at the supraglenoid tubercle.

There are two kinds of cartilage in the glenohumeral joint. The first type is the white cartilage at the end of bones (called articular cartilage) that allows them to slide and move on each other. When this type of cartilage starts to wear out, which is called arthritis, the joint becomes painful and stiff. The labrum, the second type of cartilage, is more fibrous or rigid than the cartilage on the ends of the ball and socket, being found only around the socket where it is attached (Seeley et al., 2007).

2.2 Bone mechanics

Bone is a highly hierarchical tissue adapted to various mechanical, biological and chemical functions that is continually being torn down and replaced by biological remodelling. The main constituent of whole bones is bone tissue and it has the functional task of withstanding substantial stress during locomotion and strenuous activities such as lifting heavy weights. There are two types of bone tissue: cortical and trabecular bone. Since bones are loaded both cylindrically and statically, fatigue and creep responses are important aspects of their mechanical behaviour. As a matter of fact, there is evidence that primary stimulus for bone remodelling is the repair of damage that accumulates from habitual cyclic loading (Burr et al., 1997; Burr, Martin, Schaffler, & Radin, 1985). Implantation of orthopedic prostheses requires strong bone for optimal fixation, a difficult requirement for sites where bone strength can be greatly compromised. Understanding the behaviour of bone tissue and its relation to hierarchical levels of organization is important to model with accuracy the behaviour of the shoulder joint and its response to physiological loads as well as to the implantation of a prosthetic component.

2.2.1 Hierarchical structure

At the nanometer scale, bone tissue is composed of inorganic (40%) and organic (35%) phases and water (25%). The inorganic phase is a ceramic crystalline-type mineral that is an impure form of naturally occurring calcium phosphate, commonly referred to as hydroxypatite, which accounts for bone stiffness and strength. The organic phase consistes primarily of type I collagen and small amounts of proteoglycans non-collagenous proteins. The collagen molecules are arranged in parallel with each other head to tail with a gap or "hole zone" where mineralization begins, extending into other intermolecular spaces and resulting in a mineralized fibril. At the microstructural level, bone can be divided into two types based on its porosity: cortical or compact bone, whose porosity varies between 5% and 10%, and trabecular or cancellous bone, which has a porosity between 50 and 95% (Figure 2.3). At

the macroscopic level, bone is heterogeneous, porous and anisotropic (Kutz, 2002).

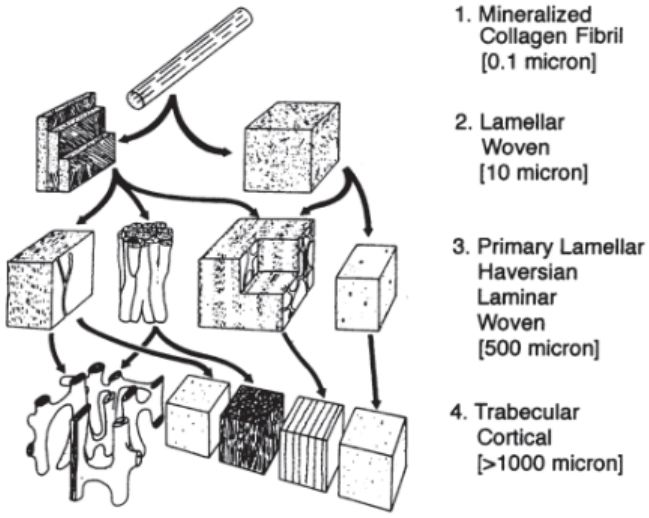

Figure 2.3: Bone tissue microstructure: from the level of mineralized collagen fibrils to cortical and trabecular bone (Wainwright et al., 1976).

2.2.2 Composition of compact bone

In the diaphysis of long bone, the microstructure of compact bone consists of an arrangement of the mineralized collagen fibrils as concentric cylindrical shaped *lamellae* forming *osteons* that surround the *Haversian canals* and are believed to be roughly aligned with the main direction of loading. These *Haversian canals* are vascular channels with about 50 μm of diameter that contain blood vessel capilaries, nerves and a variety of bone cells. There are also *Volkmann's canals* that are similar in diameter to the *Haversian canals* but run transverse to the diaphyseal axis, providing a radial path for blood flow within the bone (Figure 2.4) (Seeley et al., 2007).

2.2.3 Composition of trabecular bone

In trabecular bone, the *lamellae* are arranged in a less well-organized way to form a network of rods and plates about 100 to 300 μm thick interspersed with large marrow spaces.

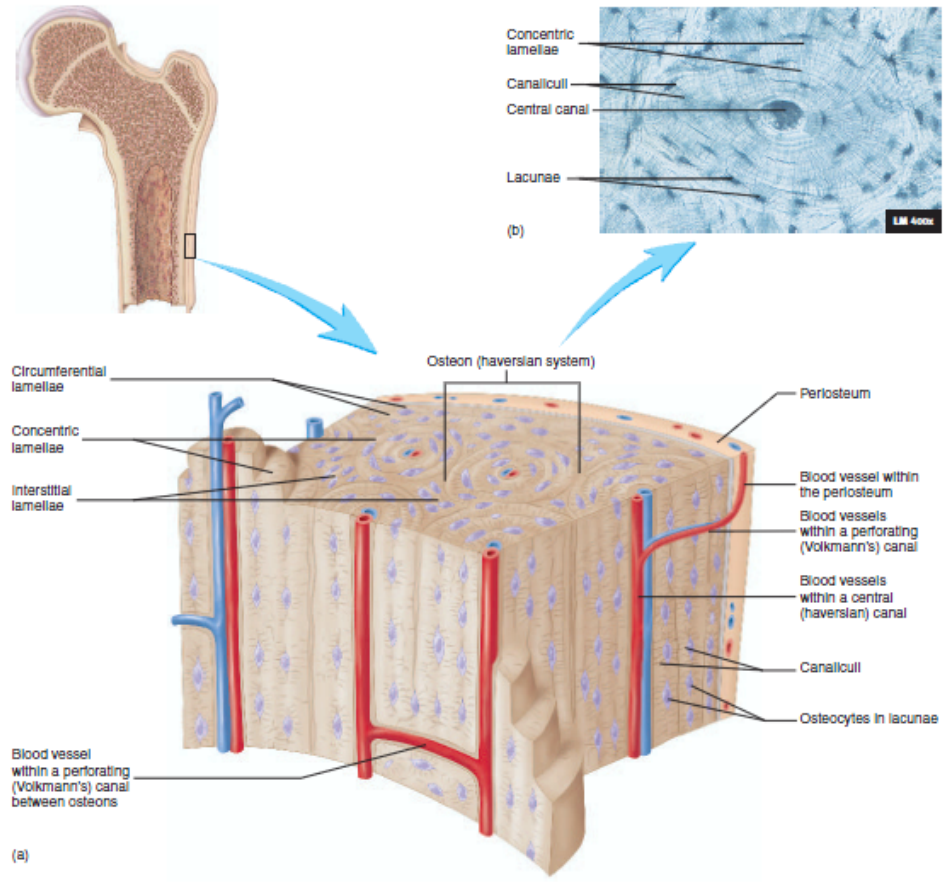

Figure 2.4: Compact bone structure: (a) consists mainly of *osteons*, which are concentric *lamellae* surrounding blood vessels within central canals. The outer surface of the bone is formed by circumferential *lamellae*, and bone between the *osteons* consists of interstitial *lamellae*. (b) Photomicrograph of an *osteon* (Seeley et al., 2007).

At the macroscopic level, this type of bone is a highly anisotropic material with complex microstructure whose porosity and composition change in response to mechanical or physiological stimuli. Its mechanical properties at the meso- and macroscale are determined by the properties of its bone tissue as well as the architectural arrangement of the individual *trabeculae*.

Apparent density is a measure defined as the ratio of the mass of bone tissue to the bulk of volume of the specimen, including the volume associated with the vascular channels and higher-level porosity and not accounting for its geometrical arrangement. Ash density is the weight of mineral phase divided by the bone volume and can be used to characterize the

relative amount of mineral in bone tissue. Bone Volume Fraction (BV/TV) is a measure of bone volume over total volume and gives a scalar architectural property that accounts for the volume occupied by the pores (Hayes & Carter, Jul 1976; Kabel, van Rietbergen, Odgaard, & Huiskes, Oct 1999; Matsuura, Eckstein, Lochmüller, & Zysset, Feb 2008).

Apparent density was shown to be the most important determinant of trabecular bone mechanical properties, however, it was also demonstrated that trabecular architecture has an important role in the inherent mechanical properties of trabecular bone. Conventional imaging techniques, such as micro-Computed Tomography (CT) allow for high resolution 3D reconstructions of trabecular structures, providing more detailed quantification of bone 3D morphology that accounts for main trabecular orientations. After segmentation of the acquired grey scale voxel data sets, it is possible to measure directly in the 3D space indices such as BV/TV, Bone Volume (BV), trabecular thickness, trabecular number and trabecular spacing (Rüegsegger, Koller, & Müller, Jan 1996).

Estimating fabric tensors is one of the most widely used techniques to characterize the microstructural architecture of materials, in particular, trabecular bone. Fabric tensors are able to estimate both anisotropy and orientation of a material with respect to another one. The Mean Intercept Length (MIL) tensor is the most used technique to estimate miscrostructure orientation and anisotropy of trabecular bone. The basic principle of this method is to count the number of intersections between a linear grid and the bone/marrow interface as a function of the grid's orientation. The mean intercept length (the mean length of the line between two intersections) is defined as the total length of the line grid divided by the number of intersections (Whitehouse, Jul 1974; Moreno, Borga, & Smedby, 2012).

2.2.4 Mechanical properties

The mechanical properties of bone tissue change depending on the structural level of interest. Regarding cortical bone, at the lamellar level the elastic moduli (see Appendix B) was measured in the range of 22 GPa, through nanoindentation tests (Rho, Tsui, & Pharr, Oct 1997; Zysset, Guo, Hoffler, Moore, & Goldstein, Oct 1999; Hengsberger, Kulik, & Zysset,

Jan 2001). On the other hand, lamellar bone in the human *trabeculae* registered an elastic modulus in the range of 11 GPa (Mazza, Franzoso, Pretterklieber, & Zysset, 2008; Roy, Rho, Tsui, Evans, & Pharr, Feb 1999).

The macroscopic apparent elastic behaviour, for both cortical and trabecular bone, is characterized by linear relationships between strains and stress (see Appendix B), registering no differences between tensile and compressive elastic constants (Röhl, Larsen, Linde, Odgaard, & Jorgensen, 1991). To describe bone properties at the microscopic level, Hooke's law is often used. This law characterizes the mechanical behaviour of linear elastic solids, relating the strains $\mathbf{E}$ to the applied stress $\mathbf{S}$: $\mathbf{E} = E\mathbf{S}$, where E is the compliance tensor. For linear elastic solids this can also expressed in terms of the stiffness tensor S: $\mathbf{S} = S\mathbf{E}$.

Cortical bone anisotropic elastic properties can be approximated by transverse isotropic or orthotropic constitutive relations (Van Buskirk, Cowin, & Ward, May 1981), in which elasticity exhibits a cubic dependence with bone volume fraction and calcium content (Currey, 1988; Kotha & Guzelsu, Dec 2003), but no considerable dependence with collagen content (Wang, Bank, TeKoppele, & Agrawal, 2001).

Trabecular bone exhibits greater porosity and so an apparent elastic modulus is often measured based on a representative volume element. To relate local strains in bone to those on the apparent level, it is necessary that this volume element is large enough to allow for a sensible definition of continuous properties. The apparent elastic modulus is approximately in the order of 0.1-2000 MPa (Keaveny, Morgan, Niebur, & Yeh, 2001). The quadratic dependence between apparent trabecular elasticity and bone volume fraction was shown in various studies, as well as the power relationship to bone mineral content that reported a coefficient ranging from 1.3 (Zysset, Sonny, & Hayes, Apr 1994) to 2.74 (Hernandez, Beaupré, Keller, & Carter, 2001). Zysset and Curnier further described the relation of apparent elastic properties of trabecular bone with bone volume fraction and fabric tensor. Their theoretical model was based on a generalized anisotropic form of Hooke's law and also on the assumption that trabecular anisotropy is due only to its structure.

Regarding the elastic limit or yield strength, this is defined as the stress at which a

material begins to deform plastically, or in the field of bone mechanics, it quantifies the damage behaviour in bone. Yield is often defined as the point at where the stress-strain curve deviates by 0.2% from the line of initial slope. The yielding behaviour of bone differs in tension and compression. For compact bone, the tensile yield stress is reported to be about 141 MPa, whereas in compression is reported to be 196 MPa. As for trabecular bone, it can only withstand small strains in the range of 1 to 7% (Keaveny, Guo, Wachtel, McMahon, & Hayes, Sep 1994), exhibiting softening and densification at large deformations.

2.3 Glenoid bone strength and material properties

Whereas the mechanical properties of cortical bone are relatively consistent among different sites, the properties of cancellous bone vary greatly. Many studies have investigated the properties of femoral and tibial cancellous bone, but only a few (Frich et al., 1997; Anglin, Tolhurst, Wyss, & Pichora, 1999) determined glenoid cancellous bone properties, particularly with respect to strength and depth. Finite element analyses used to model the response of the glenoid to implant prosthesis were therefore all based on assumptions that the material properties of glenoid bone were similar to those of the tibial plateau. In the work done by Anglin et al. the mean strength and modulus throughout the cancellous glenoid vault of ten glenoids was determined as being 10.3 MPa and 99 MPa, respectively. Since strength and modulus decrease with age and the used specimens were older, these values are considered appropriate for prosthesis design. The postero-superior region was determined as the strongest one and the central column (that agrees with the keel position in many glenoid components) was considered weaker than both anterior and posterior regions but deeper. This was also shown in Frich et al., were the superior part of the Glenoid registered 400 MPa of elastic modulus. A large drop in strength and modulus below subchondral layer was also observed, emphasizing the importance of maintaining this layer during prosthetic replacement.

The average anisotropy ratio was found to be 5.2 in the work performed by Frich et al.,

which indicates strong anisotropy. The apparent density of the glenoid was on average 0.35 $g.cm^{-3}$ and the Poisson's ratio (see Appendix B) averaged 0.263.

2.4 Finite element method

The FE method is a numerical technique for finding approximate solutions to boundary value problems that are modelled by differential equations. It uses the calculus of variations to minimize an error function and produce a stable solution. The FE method holds all the methods for connecting many simple element equations over many small subdomains - finite elements - to approximate a more complex equation over a large domain. The subdivision of a whole domain into simpler parts has many advantages, such as the accurate representation of complex geometry, the inclusion of dissimilar material properties and easier representation of the total solution (Strang & Fix, 1973).

Typically this method involves, firstly, the use of mesh generation techniques for dividing the main domain into a collection of subdomains (Figure 2.5), each one represented by a set of element equations related to the original problem, and secondly, the systematic recombination of all sets of element equations into a global system of equations for the final calculation. This global system of equations has known solution techniques and can be calculated from the initial values of the original problem in order to obtain a numerical answer (Strang & Fix, 1973).

In biomechanics, the advent of high-resolution finite-element modelling has led to enormous progress in determining elastic stiffness matrices, multiaxial failure behaviour and trabecular tissue properties, for example (van Rietbergen, Weinans, Huiskes, & Odgaard, 1995). FE models of individual specimens, developed using micro-computed tomography (Kinney, Lane, & Haupt, 1995; Kuhn, Goldstein, Feldkamp, Goulet, & Jesion, 1990) and other types of microscopic imaging (Odgaard, 1997; Beck et al., 1997) have been used to compute the full set of elastic constants for specimens from multiple anatomic sites (Kutz, 2002).

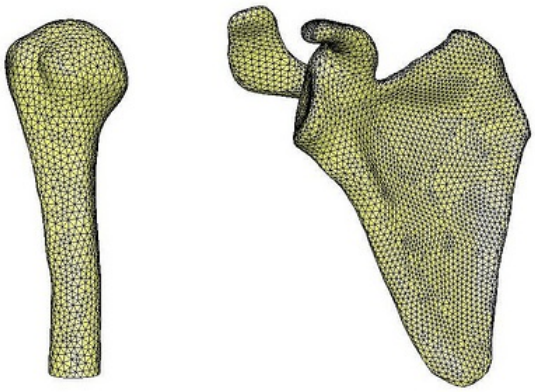

Figure 2.5: FE meshes of the human humerus and scapula (adapted from Nelson Ribeiro, www.flickr.com, 2009).

2.4.1 Elements

An element can be characterized by the family at which it belongs, its degrees of freedom, the number of nodes, its formulation and integration.

Figure 2.6 shows the element families most commonly used in a stress analysis. One of the major distinctions between different element families is the geometry type that each family assumes.

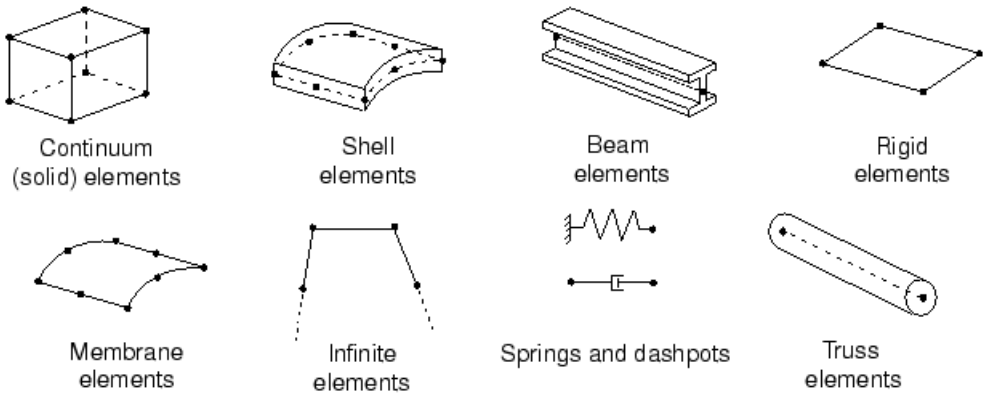

Figure 2.6: Commonly used element families (Abaqus Analysis User's Guide).

The degrees of freedom are the fundamental variables calculated during the analysis. For a stress/displacement simulation the degrees of freedom are the translations and, for shell, pipe, and beam elements, the rotations at each node.

Displacements and other degrees of freedom are calculated at the nodes of the element. At any other point in the element, the displacements are obtained by interpolating from the nodal displacements. Usually the interpolation order is determined by the number of nodes used in the element, as illustrated in the examples in Figure 2.7.

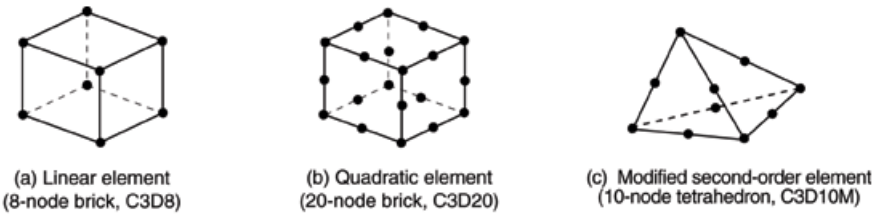

Figure 2.7: Linear brick, quadratic brick, and modified tetrahedral elements (Abaqus Analysis User's Guide, http://50.16.176.52/v6.13/).

Elements that have nodes only at their corners, such as the 8-node brick (Figure 2.7(a)), use linear interpolation in each direction and are often called linear elements or first-order elements. Elements with midside nodes, such as the 20-node brick (Figure 2.7(b)), use quadratic interpolation and are often called quadratic elements or second-order elements. Modified triangular or tetrahedral elements with midside nodes, such as the 10-node tetrahedron (Figure 2.7(c)), use a modified second-order interpolation and are often called modified elements or modified second-order elements.

An element's formulation refers to the mathematical theory used to define the element's behaviour. In the Lagrangian, or material, description of behaviour the element deforms with the material. On the other hand, in the alternative Eulerian, or spatial, description elements are fixed in space as the material flows through them. Eulerian methods are used commonly in fluid mechanics simulations and Lagrangian in stress/displacement analyses. However, software such as Abaqus/Explicit, offers multimaterial Eulerian elements for use in stress/displacement analyses and also adaptive meshing that combines both formulations and allows the motion of the element to be independent of the material (Abaqus Analysis User's Guide, http://50.16.176.52/v6.13/).

Abaqus uses numerical techniques to integrate various quantities over the volume of each element, thus allowing complete generality in material behaviour. Using Gaussian

quadrature for most elements, it evaluates the material response at each integration point in each element. Some continuum elements in Abaqus can use full or reduced integration, a choice that can have a significant effect on the accuracy of the element for a given problem.

Each element in Abaqus has an unique name that identifies the primary element characteristics mentioned previously (Figure 2.8).

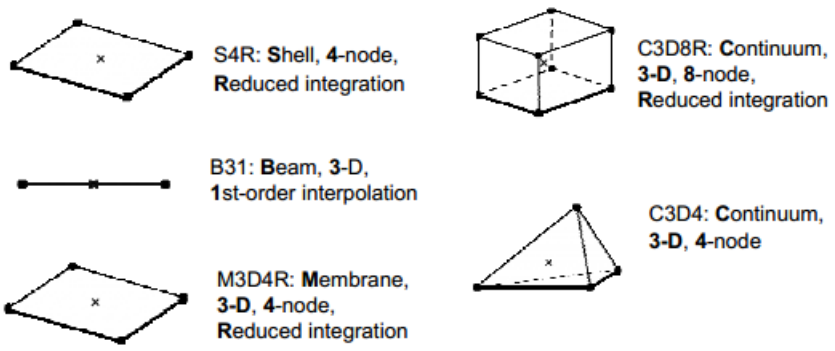

Figure 2.8: Examples of elements and their names' meaning in Abaqus (Abaqus Analysis User's Guide, http://50.16.176.52/v6.13/).

Continuum stress/displacement elements in Abaqus have names that begin with the letter "C". The next two letters indicate the dimensionality and usually, but not always, the active degrees of freedom in the element. The letters "3D" indicate a three-dimensional element; "AX", an axisymmetric element; "PE", a plane strain element; and "PS", a plane stress element. Three-dimensional continuum elements can be hexahedra (bricks), wedges, or tetrahedra.

Given the wide variety of element types available, it is important to select the correct element for a particular application. This choice can be simplified by considering specific element characteristics such as: first- or second-order; hexahedra/quadrilaterals or tetrahedra/triangles.

In first-order plane strain, generalized plane strain, axisymmetric quadrilateral, hexahedral solid elements, and cylindrical elements, the strain operator provides constant volumetric strain throughout the element. This constant strain prevents mesh "locking" when the material response is approximately incompressible.

Second-order elements provide higher accuracy in Abaqus/Standard than first-order elements for "smooth" problems that do not involve severe element distortions (Abaqus Analysis User's Guide, http://50.16.176.52/v6.13/). They capture stress concentrations more effectively and are better for modelling geometric features: they can model a curved surface with fewer elements. Finally, second-order elements are very effective in bending-dominated problems.

Triangular and tetrahedral elements are geometrically versatile and are used in many automatic meshing algorithms. It is very convenient to mesh a complex shape with triangles or tetrahedra, and the second-order and modified triangular and tetrahedral elements (CPE6, CPE6M, C3D10, C3D10M, etc.) in Abaqus are suitable for general usage. However, a good mesh of hexahedral elements usually provides a solution of equivalent accuracy at less cost. Quadrilaterals and hexahedra have a better convergence rate than triangles and tetrahedra, and sensitivity to mesh orientation in regular meshes is not an issue. However, triangles and tetrahedra are less sensitive to initial element shape, whereas first-order quadrilaterals and hexahedra perform better if their shape is approximately rectangular. The elements become much less accurate when they are initially distorted.

2.4.2 Mesh convergence

It is important to use a sufficiently refined mesh to ensure that the results from the simulation are adequate. Coarse meshes can yield inaccurate results in analyses. The numerical solution provided by the model will tend toward a unique value as the mesh density increases. The computer resources required to run the simulation also increase as the mesh is refined. The mesh is said to be converged when further mesh refinement produces a negligible change in the solution.

Figure 2.9 shows four meshes with different refinement levels for a connecting lug. It is always good practice to perform a mesh convergence study, where the same problem is simulated with a finer mesh and the results are compared.

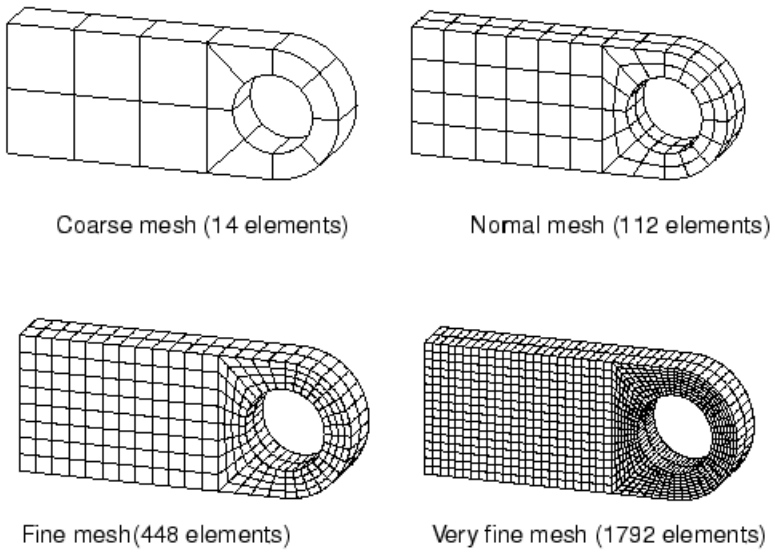

Figure 2.9: Different meshes for connecting lug problem featured in Abaqus (Abaqus Analysis User's Guide, http://50.16.176.52/v6.13/).

Chapter 3

State of the art

3.1 Total shoulder arthroplasty

Shoulder replacement surgery was first performed in the United States in the 1950s to treat severe shoulder fractures. Over the years, shoulder joint replacement became used in the treatment of many other painful conditions of the shoulder, such as osteoarthritis, rheumatoid arthritis, severe fracture or avascular necrosis that limit the ability to move the arm.

Although shoulder joint replacement is less common than knee or hip replacement, nowadays about 53 000 people in the US have this type of surgery every year, according to the Agency for Healthcare Research and Quality.

There are different types of shoulder replacement, such as the total arthroplasty, the stemmed and resurfacing hemiarthroplasty and the reverse total shoulder arthroplasty. In this thesis, the procedure being studied is the TSA (Figure 3.1). This technique involves replacing the arthritic joint surfaces with a highly polished metal ball attached to a stem (the humeral component), and a plastic socket (the glenoid component). These components come in various sizes and may be either cemented or "press fit" into the bone, depending on its quality. If the glenoid cavity is healthy or the bone is severely damaged, the implantation of a glenoid component is not advised.

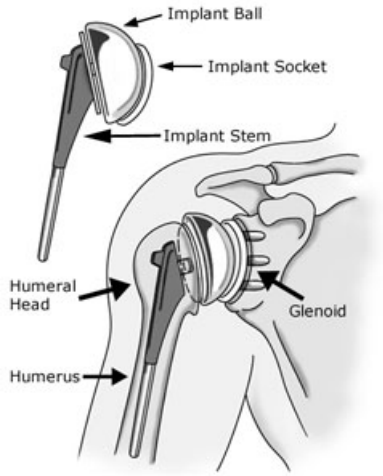

Figure 3.1: Anatomical total shoulder arthroplasty (*Soulder Joint Replacement*, OrthoInfo, http://orthoinfo.aaos.org/).

Complications after shoulder arthroplasty may include infection, instability, neurovascular injury, stiffness, cuff tear, periprosthetic fractures, glenoid erosion and component loosening. However, the risk of glenoid loosening seems to have decreased with improvements in implant design and surgical technique, as shown in results of revision surgery (Sanchez-Sotelo, Mar 2011).

The results of shoulder arthroplasty vary depending on the underlying diagnosis, the condition of the joint and the soft-tissues at the time of surgery, and the type of reconstruction performed. The results of shoulder arthroplasty in primary osteoarthritis, for example, are satisfactory in a large number of patients: pain is improved in over 90% of the individuals, and their average elevation is usually over 135 degrees. Considering this particular diagnosis, TSA seems to be superior to hemiarthroplasty. This was clearly shown in a prospective randomized study by Garstman et al. (Gartsman, Elkousy, Warnock, Edwards, & O Connor, May 2005) and a long-term 15 year study by Sperling et al. (Sperling, Cofield, & Rowland, 2004). The same outcome was observed in patients that suffered of osteonecrosis (Hattrup & Cofield, 2009) and inflammatory arthritis (Sperling et al., 2004).

Overall, shoulder arthroplasty is a very successful procedure with predictable pain relief and substantial improvements in motion and function.

3.1.1 The glenoid component

In the early 1970s, Dr. Charles Neer introduced the first glenoid component. He proposed a final design of an all-polyethylene component that was keeled and cemented, with conforming humeral and glenoid radii of curvature. Later in 1982, Dr. Neer was the first author to report successful pain control following total shoulder replacement surgery (Neer, Watson, & Stanton, Mar 1982).

Although glenoid replacement has improved patient satisfaction, pain control, and clinical outcomes, there remains concern regarding the longevity of the glenoid component, which may be considered the weak link of a total shoulder replacement. Glenoid loosening is the primary reason for failure after TSA, accounting for 32% of complications after surgery (Bohsali, Wirth, & Rockwood, Oct 2006).

The glenohumeral joint is characterized as a nonweight-bearing joint, however it is subject to forces that may exceed body weight. In an investigation involving instrumented joint replacements in four patients, Westerhoff et al. (Westerhoff et al., 2009) reported that peak glenohumeral contact forces averaged 76% body weight during hair combing and 123% body weight while setting down a coffee pot. Besides, these forces often are transmitted between the humeral head and the glenoid at eccentric locations on the glenoid surface.

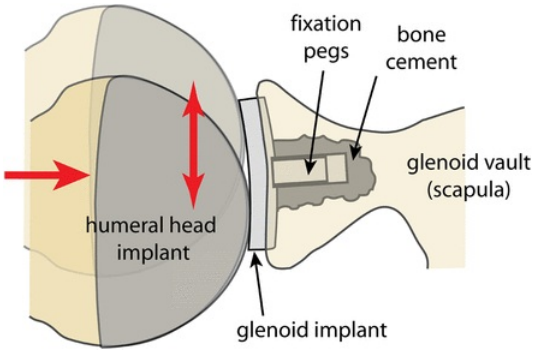

Figure 3.2: The primary mechanism of glenoid loosening involves repeated, eccentric forces of the humeral head on the glenoid rim, so-called rocking-horse loading (Armstrong & Lewis, 2013).

The ”rocking-horse” phenomenon (Figure 3.2) induced by eccentric loading is commonly

attributed to loosening of the glenoid component because it causes compressive stresses at the fixation surface when the external load is applied at the superior or inferior edge of the glenoid component, as well as tensile stresses on the opposite end (Franklin, Barrett, Jackins, & Matsen, 1988; Wirth & Rockwood, 1996). How this phenomenon affects the mechanics of a bone-implant system and, consequently, affects failure still remains unclear.

This lack of understanding is in large part responsible for the broad array of glenoid implant designs that have been developed in an effort to decrease the rate of loosening (Figure 3.3). Keels and pegs are commonly used as fixation features and a metal backing is incorporated in some designs in order to supplement fixation between the implant and the bone with or without the use of cement.

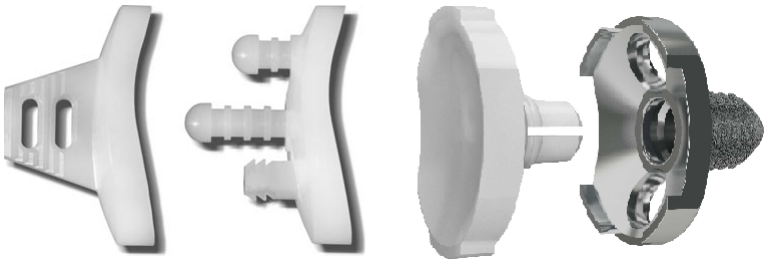

Figure 3.3: Different glenoid components designs (from left to right): keeled, pegged and pegged with metal backing (adapted from Common US Shoulder Prostheses, http://depts.washington.edu/).

Non-metal-backed designs have a greater survival rate than metal-backed designs, and pegged designs have a lower incidence of radiolucency than keeled designs. Although better fixation has been suggested with cemented and pegged implants, the rate of radiolucencies is still as high as 36% to 83% with these commonly used designs, consistent with high aseptic loosening rates (Patel, Wright, & Gao, 2014).

Anatomical and biomechanical considerations

The normal adult glenoid is a slightly concave, oval, non constrained articular surface with a larger superior-inferior diameter, that measures approximately 35 mm, and an anterior-posterior Anterior-Posterior (AP) diameter that measures approximately 25 mm (Brems,

1993; Ibarra, Dines, & McLaughlin, Jul 1998).

Prosthetic glenoid components cannot reproduce the exact geometry and mechanical properties of the native glenoid. There is a significant mismatch between the surface area of the glenoid and the humeral head: in the normal glenohumeral joint, the radius of the glenoid curvature is slightly larger than that of the humeral head curvature, allowing some translation of the humeral head on the glenoid. The malleable labrum and cartilage make the glenoid curvature more conforming to the humeral head while aiding the stability of the joint. A polyethylene glenoid component is much stiffer than the labrum and cartilage. If the radii of curvatures are equal between the glenoid and humeral head components it is called conforming design and the head is held precisely in the center by concavity compression with no head translation. Although this exact conformity provides excellent stability, it has the risk of eccentric loading on the periphery during head translation on the glenoid, causing wear and loosening of the glenoid component. On the other hand, there is the non-conforming design, in which the glenoid radius of curvature is slightly larger. In this radial mismatch, the humeral head is allowed to translate before being lifted off of the glenoid component. The disadvantage is that this mismatch decreases the contact area, thus increasing the contact stress with increased risk of polyethylene wear and failure, especially if the radial mismatch exceeds 10 mm, as well as decreasing the joint stability. Recently a hybrid design was introduced for the glenoid component with a conforming center and a nonconforming periphery, combining the advantages of both previous designs (Zhang et al., Mar 2013).

The glenoid is normally retroverted approximately 5° and tilted superiorly approximately 5° with respect to the scapula. The scapula is anteverted approximately 30° with respect to the chest wall. There is only a small amount of cancellous bone present at the base of the caracoid process that supports the glenoid component. Insufficient bone in this region compromises glenoid component fixation.

Eccentric glenohumeral loading can result in asymmetric glenoid wear and an increase in glenoid tilt. When there is rotator cuff insufficiency, the biomechanical stresses caused

by unopposed deltoid forces result in superior migration of the humeral head, causing its articulation with the superior lip of the glenoid and therefore resulting in superior glenoid wear. Osteoarthritis and AP instability can result in posterior erosion, with decreased surface area of the glenoid and its vault. In the same way, rheumatoid arthritis generally results in loss of bone and medial migration of the joint line to the base of the caracoid process.

Such pathologic changes in the normal anatomy of the glenohumeral joint must be considered when planning the surgical procedure. In some cases, when there is mild deformity, eccentric reaming or excision of the proud surface are usually necessary. As for moderate deformities, this may require bone graft, customized glenoid prosthesis or even alteration in the amount of retroversion of the humeral component for good results (Ibarra et al., Jul 1998).

Fixation

Most glenoid components are fixed with PMMA. The traditional component is an all-polyethylene implant with a slightly convex backside and a keel to be inserted into the glenoid vault. Some components currently used have their keel replaced by two or more pegs. There are multiple peg configurations. Some components are designed for hybrid fixation, where one of the pegs is designed for ingrowth and fabricated as either a grooved all-polyethylene peg or a metal ingrowth peg. Pegged components seem to allow more accurate preparation of the glenoid bone and have been associated in some studies to a lower rate of radiolucent lines in the immediate postoperative radiograph (Lazarus, Jensen, Southworth, & Matsen, 2002). However, in some patients with bone loss it is not possible to implant a pegged component.

Glenoid component fixation, in general, can be divided into three main categories: cemented, cementless, and hybrid. The cemented glenoid component design remains the standard for total shoulder arthroplasty. Cementless fixation remains an attractive alternative, but unfortunately the first generation of uncemented implants were associated with a high failure rate (Boileau et al., 2002). These components had relatively thin polyethylene inserts in order to avoid overstuffing of the glenohumeral joint, and they reported polyethylene wear

or dissociation. New materials such as porous titanium or tantalum may allow manufacturing of more successful cementless glenoid components in the future (Sanchez-Sotelo, Mar 2011). As concern regarding glenoid component longevity remains, newer hybrid designs for fixation are evolving.

3.2 Finite element modelling

FE modelling has been an effective tool in the field of bone mechanics to predict the behavior of bone material under different loading situations and to evaluate the effects of implant-related factors on the risk of fracture and loosening. Two main modelling approaches can be identified: 1) the *classical finite element approach*, where bone structures are modeled with homogenized materials accounting for local variations in bone density; 2) the *micro-finite element (μFE) approach*, in which the complex geometrical structure of bone is modeled explicitly by including the trabecular structure and cortical shell through conversion of CT voxels to finite elements, after segmentation of bone voxels.

3.2.1 The classical FE approach

Classical FE models use homogenization methods to describe trabecular bone as a continuum, i. e. without an explicit description of trabecular architecture. This approach relies on the concept of Representative Volume Element (RVE), a sub-region of bone in which the local apparent mechanic properties are defined on the mesoscale level. Properties in these RVEs are described in relation to average mesoscale bone density and architecture within the RVE, and it is possible to vary these properties across the bone, in this case the glenoid region of the scapula.

Friedman et al. (Friedman, LaBerge, Dooley, & OHara, 1992) was one of the first to investigate the stress distributions caused by various loading conditions using a two-dimensional plane stress model of the natural glenoid. In this study, a mesh of isoparametric quadrilateral and triangular elements was used and bone was assumed to be a homogeneous isotropic

structure divided in 4 bone regions (1 outer cortical layer and 3 inner cancellous bone layers). Similarly, Lacroix et al. (Lacroix & Prendergast, 1997), preformed a two-dimensional plane stress finite element analysis to study bone response to various designs of cemented glenoid component (Figure 3.4).

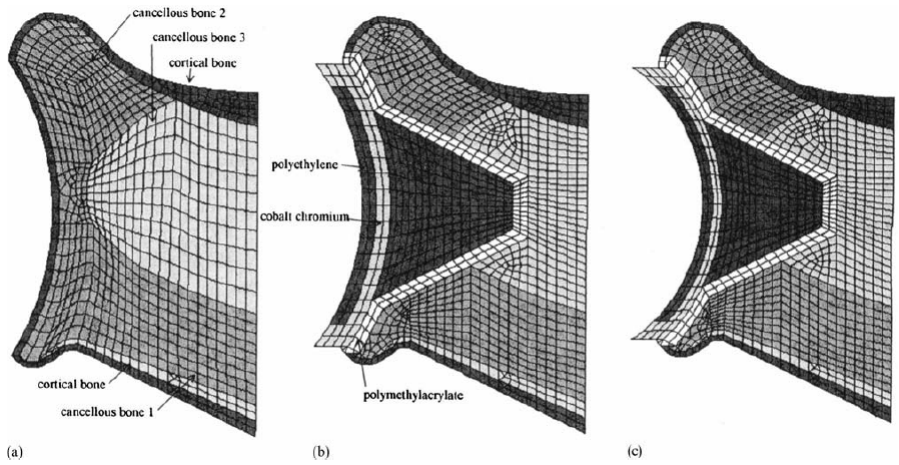

Figure 3.4: Finite element mesh used in Lacroix et al.: (a) the intact glenoid, (b) the glenoid provided with a low constraint metal-backed prosthesis and (c) the glenoid provided with a high constraint metal-backed prosthesis (Lacroix & Prendergast, 1997).

The load transfer and stress distribution across the scapula had not been discussed "accurately" until Gupta et al., 2004 (Gupta & van der Helm, 2004). Previous studies that were mostly restricted to 2D and 3D models of the implanted glenoid were unable to describe it (Friedman et al., 1992; Lacroix & Prendergast, 1997; Lacroix, Murphy, & Prendergast, 2000; Couteau et al., 2001). These models lacked the ability to describe the complex geometry and loading adequately because other important bony structures, joints and the effect of muscles, ligaments, and joint reaction forces were omitted. The 3D model of Lacroix et al. (1997) and Lacroix et al. (2000), using CT scan data, was an effort in this direction. However, the quality of mesh generation was considered to be coarse. Furthermore, neither a validation nor the errors in the FE model was discussed, making it difficult to assess the accuracy of the results. Gupta et al. used a 3D FE model that combined shell and solid elements and a musculoskeletal shoulder model of forces developed by van der Helm, 1994.

Recent studies continued to use 3D models based on CT scans, generally with meshes of

second order tetrahedral elements, considering bone as a linear material with non-homogeneous properties related to its density, which was derived from CT data (Terrier et al., 2005; Terrier, Büchler, & Farron, 2006; Hopkins, Hansen, Amis, & Emery, 2004; Yongpravat et al., 2013; Zhang et al., Mar 2013; Patel et al., 2014). Bone-cement and implant-cement interfaces were always considered fully bonded, whereas in some cases the bone-cement interface was also considered fully debonded (Terrier et al., 2005).

3.2.2 The micro-FE approach

Micro-FE approaches have been used and developed extensively in the past few years to investigate the relations between morphology and apparent elastic, yield and post-yield behaviour of trabecular bone. The advantages of these models are the possibility of incorporating the full trabecular architecture, they account for cancellous bone anisotropy related to the bone structure and do not require relationships to convert bone density to continuum-level bone properties.

So far, micro-FE studies regarding the fixation stability and load distribution on the glenoid replacement have not yet been preformed, which is believed to be related to the limitations of this approach.

Some of the limitations are the scanning resolution and the size of the reconstructed voxels that affect the approach's accuracy. The thickness of individual *trabeculae* is on the order of 200 μm, and for that reason micro-FE studies with resolutions of 82 μm might not describe the mechanical behaviour or the underlying trabecular structure accurately. Moreover, FE predictions of apparent modulus were reported to be strongly affected by the threshold used for segmentation of CT data to create the FE mesh, causing overestimation in apparent properties. It seems evident that such an approach also requires computational efforts that increase with the size of the numerical problem, inducing large computation times and costs. Although calculations times have been reduced with the use of supercomputers enabling the distribution of the analysis over multiple processors, these are still not easily accessible. Finally, another important disadvantage of this modelling approach is that it

needs high-resolution micro-CT images and these imaging techniques are not available for all anatomic sites (Chevalier, 2008; Chevalier et al., 2007).

Chapter 4

Materials and Methods

This chapter presents the methodologies used in this thesis (Figure 4.1), from the preparation of the specimens that will be used in the experimental testing, describing the virtual implantation of the glenoid prosthetic component in a CT scan image and explaining the classical and Micro-FE models as well as the different simulated cases. Finally an overlook on the mechanical setup that will be used in the models' validation is presented.

Table 4.1 presents the software used to generate both classical and micro-FE approaches. All steps related to image processing, positioning of the glenoid components or creation of the FE models were done using a custom-made tool available at the laboratory - yBones - that was specifically designed to use in numerical biomechanics (Chevalier, Pahr, & Zysset, 2009).

4.1 Specimens preparation and scanning

In this study four shoulder joint cadaver specimens were used. The latter were from 2009, from two patients whose age and gender are unknown. However, considering the specimens' bone dimensions and condition, it is believed that the patients were old and of different gender. All specimens were scanned with Magnetic Ressonance Imaging (MRI) and posteriorly dissected with the help of a trauma surgeon to isolate the scapular bone (Figure

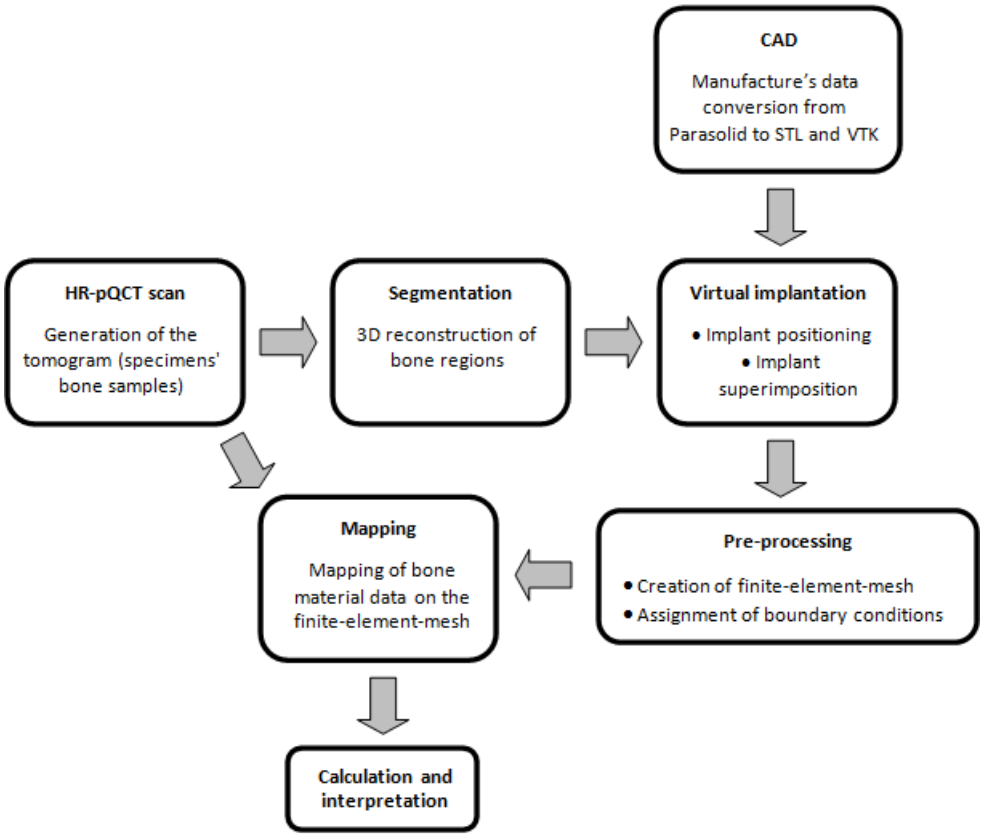

Figure 4.1: General steps of the methodology used to study the glenoid component in TSA using two different FE approaches.

Table 4.1: Software used for generating the presented FE models.

Purpose	**Software**	**Manufacture/Distributor**
Segmentation	yBones	Yan Chevalier
CAD	Solidworks	Dassault Systèmes, RI, USA
Mapping	yBones	Yan Chevalier
Pre-processor	yBones	Yan Chevalier
Solver	ABAQUS (Classical FE)	Dassault Systèmes, RI, USA
	ParFE (μFE)	Uche Mennel et al., ETH Zurich, Institute of Computational Science
Post-processor	ABAQUS Viewer (Classical FE)	Dassault Systèmes, RI, USA
	yBones (μFE)	Yan Chevalier

4.2a and b). During the dissection, some portions of the scapular blade were removed (Figure 4.2c) to allow the positioning of the specimen inside a 100 mm diameter scanning tube (Figure 4.3). This will therefore enable the scanning of the scapula using a High-Resolution Peripheral QCT (HR-pQCT) system (XtremeCT, 59.4kV, 1000μA, Scanco Medical, AG., Zurich, Switzerland) at 82 μm resolution.

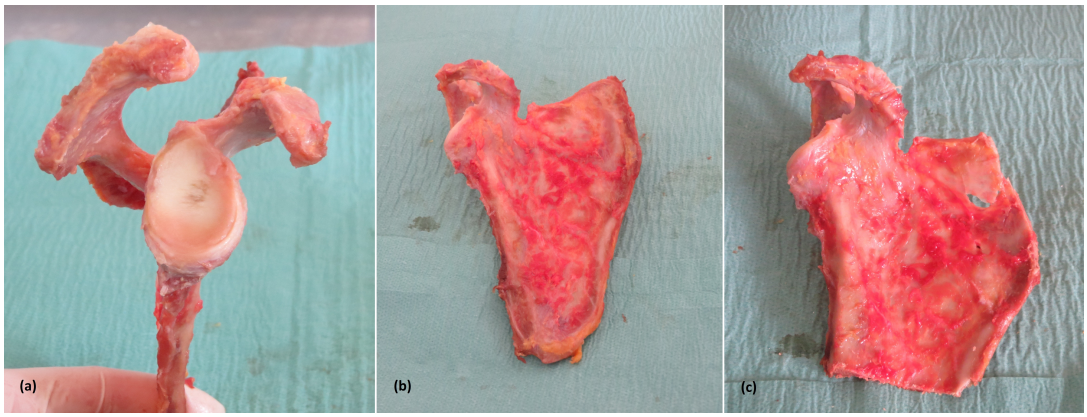

Figure 4.2: Specimens dissection: (a) close up of the glenoid with caracoid process and acromion, (b) dissected scapula, (c) scapula after cut of the medial border and inferior angle portions of the scapular blade.

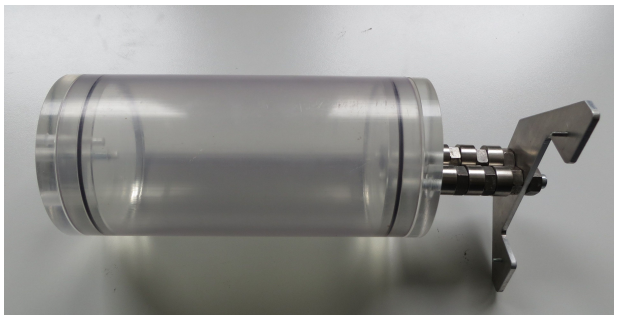

Figure 4.3: Custom-made tube designed to hold an embedded scapula inside the XtremeCT scanner.

The Superior-Inferior (SI) and AP dimensions of the specimens' glenoids are presented in Table 4.2. The measurements were made with a calliper and as we can verify, the glenoid sizes range from 37.70 mm to 43.00 mm in the SI direction. This dimensions will be used afterwards to choose the correct size of the glenoid component to be implanted.

Table 4.2: Glenoid size of specimens K3 (A and B being the left and right shoulder, respectively) K4 (A and B being the right and left shoulder, respectively).

Specimen	**Dimension**	**Measurement (mm)**
K3A	SI	42.60 ± 0.05
	AP	31.70 ± 0.05
K3B	SI	43.00 ± 0.05
	AP	30.75 ± 0.05
K4A	SI	38.90 ± 0.05
	AP	29.20 ± 0.05
K3B	SI	37.70 ± 0.05
	AP	27.40 ± 0.05

In order to avoid displacement of the specimens inside the scanning tube and get proper HR-pQCT images, the distal end of the scapular blade from each specimen was potted in a custom made cylinder with PMMA (Figure 4.4). The cylinder was made out of PVC with an inner diameter of 100 mm to match the inner diameter of the scanning tube and allow the fitting of the embedded specimen.

Figure 4.4: Embedding of specimen in PMMA, using a PVC cylinder.

4.2 Virtual implantation of anatomical glenoid components

The computed assisted drawings of the anatomical glenoid components were geometrically positioned over the geometrical bone image according to the surgical guidelines of the manufactures. The prostheses (Equinoxe Glenoids, Exactech) were a 4-pegged, asymmetric, all-polyethylene implant and a keeled, all-polyethylene implant, both available in tree sizes (small, medium and large) and with an alpha radius of curvature (Figure 4.5).

Figure 4.5: Anatomical glenoid components: pegged and keeled designs (Exactech equinoxe glenoids, http://www.exac.com/).

These glenoid components have an anatomic pear shape design and multiple features to facilitate cement interdigitation and reduce the risk of glenoid loosening. Alpha and beta glenoid curvatures enable any head size to be paired with any glenoid size while maintaining an optimal radial mismatch of approximately 5.5 mm. Table 4.3 resumes the different glenoid component sizes provided by Exactech, Inc.

The bone image used in the virtual implantation was a HR-pQCT image of the glenoid region only (the scapular blade, the caracoid process and the acromion were removed before scanning). This specimen was scanned at 82 μm resolution during previous studies with the same XtremeCT scanner mentioned previously. Since our main interest is to observe stress distribution around the implant, the HR-pQCT image was cut to isolate only the glenoid region. From the available glenoid component sizes, the large one adjusted better to this glenoid.

Table 4.3: Equinoxe glenoid: available head sizes and glenoid curvatures (Exactech, http://www.exac.com/)

	Head size (mm)	**Glenoid Curvature**
Small	38	
Medium	41	Alpha
Large	44	
Small	47	
Medium	50	Beta
Large	53	

The small glenoid implant files were first converted from a Parasolid to an ASCII STereoLithography (STL) and Visualization Toolkit (VTK) file formats using a CAD software (SolidWorks Premium 2013 x64 Edition). In order to position the implants correctly, geometrical transformations were applied to both implant designs (keeled and pegged): first a rotation in the x, y and z directions and a 1.16 scaling factor to obtain the large implant design dimensions; then a translation in the x, y and z directions. The 3D VTK model was converted to a 3D voxel file image, to which a filling algorithm was applied. The virtual implantation was completed by superimposing the resulting filled 3D voxel image of the implant with a filled image of the glenoid (a filling algorithm was also applied to the HR-pQCT image of the glenoid).

The methodology described above was used for both classical and micro-FE approach, with the exception of the filling algorithm applied to the HR-pQCT glenoid bone image. In the μFE approach the latter step was not preformed to maintain the trabeculae structural data of bone. The virtual implantation resulting images, for both numerical approaches and both implant designs, are presented in Figure 4.6.

During the TSA surgical procedure, anatomic correction of glenoid version is often necessary in order to allow a better contact between the implant and the underlying glenoid bone. To model such a scenario, the bone was virtually reamed using a spherical image mask (Figure 4.7) and then merged with the two implant designs (Figure 4.8).

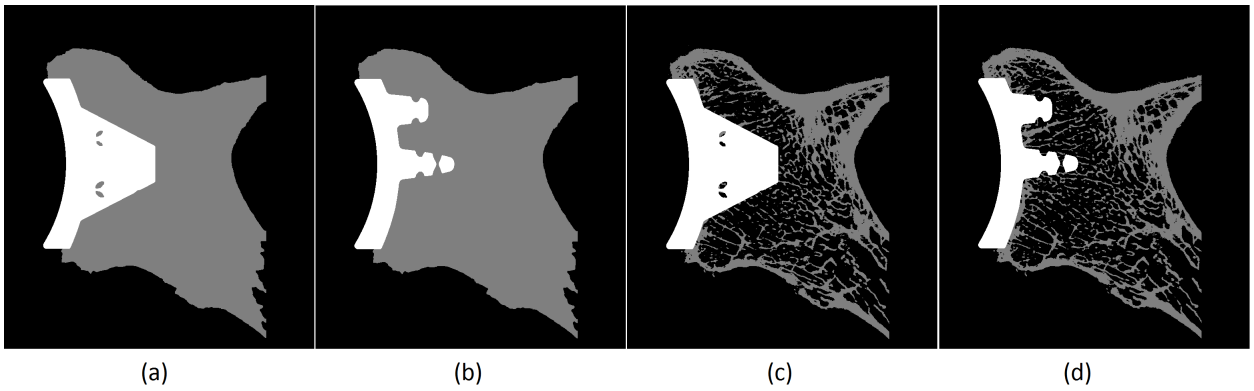

Figure 4.6: Virtual implantation, frontal anatomical cut: (a) filled glenoid bone merged with keeled implant design, (b) filled glenoid bone merged with pegged implant design, (c) unfilled glenoid bone merged with keeled implant design, (d) unfilled glenoid bone merged with pegged implant design.

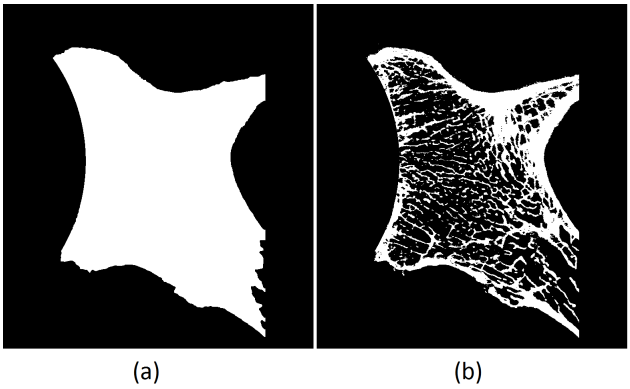

Figure 4.7: Glenoid surface after bone ream, frontal anatomical cut: (a) filled glenoid bone (b) unfilled glenoid bone.

4.3 Classical FE model

A volume mesh consisting of 1.0 mm first-order tetrahedrons (C3D4) was created from the resulting superimposed image (bone and implant). Two other separated meshed regions were created, one considering only bone (Figure 4.9) and another considering solely the implant. The segmented bone region corresponds to the elements that belong only to the bone, i.e. excluding the elements that were replaced by the keel and pegs from each implant design. By meshing the merged bone and implant image, a coherent final mesh is obtained, with element nodes that match within each other in the bone-implant interface.

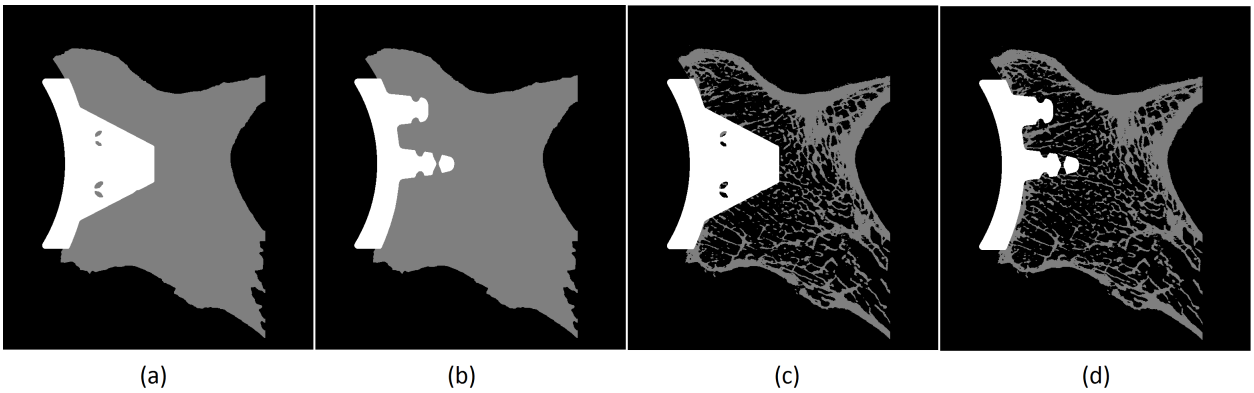

Figure 4.8: Virtual implantation after bone ream, frontal anatomical cut: (a) filled glenoid bone merged with keeled implant design, (b) filled glenoid bone merged with pegged implant design, (c) unfilled glenoid bone merged with keeled implant design, (d) unfilled glenoid bone merged with pegged implant design.

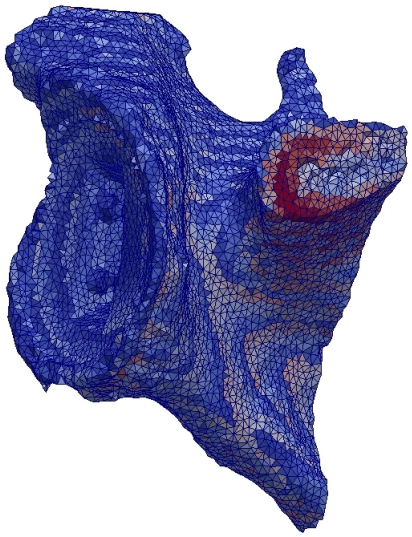

Figure 4.9: Meshed bone region resulting from virtual implantation of the keeled implant design, with assigned material properties.

Nonlinear material properties for bone were assigned based on existing material properties and described based on local Bone Mass Density (BMD) and microarchitecture mapped from the HR-pQCT image (Figure 4.10). Trabecular bone elasticity of each element was modelled

using an elastic stiffness tensor, which is created by using the following relationship:

$$E = E_0 \rho^k \tag{4.1}$$

Where ρ is the individual voxel's volume fraction calculated from the HR-pQCT image, k is an exponent set to 2.0 and E_0 is the bone tissue elastic modulus of 10000 MPa. Thus, bone tissue was modelled as isotropic and linearly elastic, with a Poisson's ratio of 0.3. Material properties for the glenoid components were assigned based on literature: an elastic modulus of 3000 MPa and Poisson's ratio of 0.3 (Chevalier, 2008).

Static FE analyses were performed in ABAQUS (version 6.13; Dassault Systèmes Simulia Corp., Providence, RI, USA).

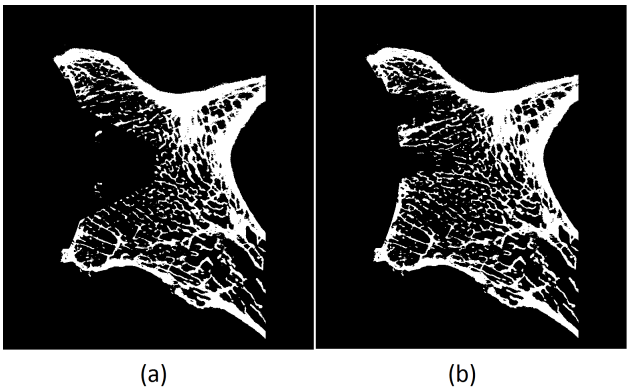

Figure 4.10: Bone image segmentation, frontal anatomical cut: (a) for virtual implantation with the keeled implant design, (b) for virtual implantation with the pegged implant design.

4.4 Micro-FE model

The resulting voxel image from the virtual implantation was converted directly into a micro-FE model (.mesh.h5 file format) using custom-made codes following an established methodology, which allowed an accurate representation of the bone structures and the implanted prosthesis using 82 μm-sized hexahedral bounded elements. Material properties were assigned with help of a parameter file, where the grey values corresponding to each different

region were associated with isotropic linear elastic properties based on literature that were given to bone (trabecular bone elasticity modelled through the elastic stiffness tensor and a Poisson's ratio of 0.3) and implant (elastic modulus of 3000 MPa and Poisson's ratio of 0.3).

The micro-FE models were solved using a dedicated open-source parallel solver (ParFE) through the university cluster.

4.5 Boundary conditions and simulated load cases

Both classical and μFE models were fixed at the cut of the scapular blade, with the nodes at this end fully constrained in all directions. A surface load was applied to a predefined region of nodes at the outer surface of the glenoid component. This region was defined through an image masking that created a cylindrical patch of 5.0 mm radius in the outer surface of the implant. Compressive displacements were applied in the y-direction until 1.0 mm, in the classical FE models, and until 0.1 mm in the μFE models, in two different loading regions: a centered region, with center in (x,y,z)=(19,0,35) mm, and an eccentric superior region, centered in (x,y,z)=(19,0,22) mm.

Implant positioning and boundary conditions were constant over the simulated cases. For the classical FE approach, four different scenarios were tested: the effect of implant design (keeled and pegged glenoid components), the effect of loading position, the effect of a cement layer and the effect of anatomic correction of glenoid version. Regarding the micro-FE approach, only two different scenarios were tested: the effect of implant design and loading position.

4.5.1 Effect of a cement layer

A cement layer was simulated around the implants and created using extrusions and boolean operations. In a similar way as for the definition of the loading region, an image masking of a dilation of the implants was overlapped with both bone and glenoid components (Figure 4.11), resulting in a 20 voxel cement layer.

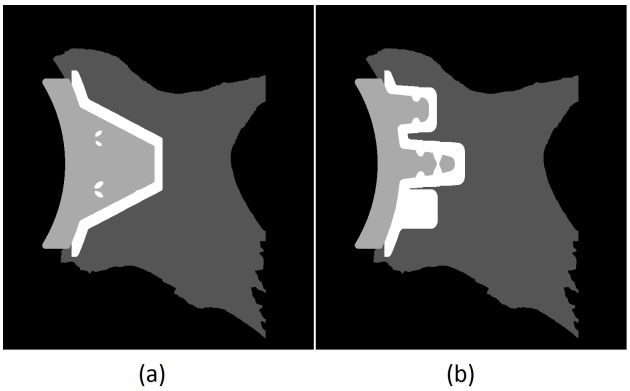

Figure 4.11: Cement layer merged with filled bone, frontal anatomical cut: (a) keeled glenoid component (b) pegged glenoid component.

A composite region corresponding to the cement layer was segmented and two different situations were modelled. In the first, voxels inside the segmented cement region were given linear orthotropic elastic properties (elastic modulus of 3000 MPa, Poisson's ratio of 0.3) described by a rule of mixture (for further information consult Chevalier, PhD Thesis). In the second, the segmented cement region was described instead as totally filled with cement.

4.6 Validation: mechanical test

The numerical methodologies used in this study will be validated through a mechanical test, first using bone models (Sawbones Inc.), and afterwards using the cadaver specimens already dissected and prepared. Similar scenarios will be tested and bone micromotions will be measured using a Linear Variable Differential Transformer (LVDT) system. The embedded specimens will be positioned accordingly with the loading cases and with help of a positioning setup.

The positioning setup (Figure 4.12) consists of a rotational plate that allows the vertical tilt of the scapula. The latter is placed inside a cylindrical tube fixed to the rotational plate. By changing the scapula orientation it is possible to correctly position the glenoid, in order for it to undergo compressive loading from the humeral head.

The CAD drawings of this setup (see Appendix A) were designed in Solidworks (Premium

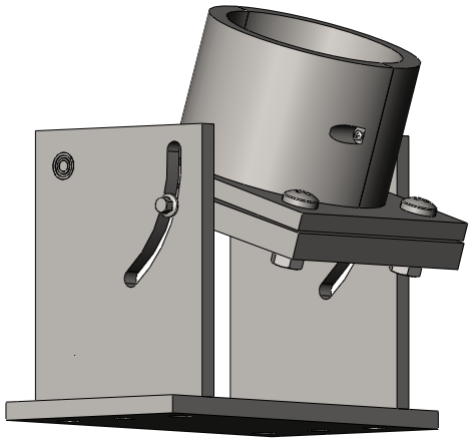

Figure 4.12: Positioning setup for the scapula.

2013 x64 Edition). The setup is made up of two main parts: one consisting of the rotating plate and its support, and other consisting of the cylindrical tube to place the scapula. The cylindrical tube can be completely disassembled in three other parts: two half cylinders and a rectangular base plate, enabling a better manipulation of the setup. The rotating plate can be fixed with the desired inclination using a screw.

Chapter 5

Results

In this chapter the results of both classical and micro-FE models, for the different implantation and loading scenarios are presented. Both qualitative and quantitative descriptions of these results are given, establishing associations and comparisons between the various simulated cases.

5.1 Classical FE model: investigation of fixation strength

In the classical FE approach four different factors were tested: the effect of an anatomic correction of the glenoid surface, the effect of implant design, the loading position and the effect of cementing. The effect of the implant design was tested for the other three scenarios, the effect of loading position was tested only considering the glenoid with surface ream, and the effect of a cement layer was tested solely for the case of centered loading position. For each simulated scenario, Table 5.1 shows the total CPU time required to solve the model.

Regarding the mesh size and quality, during the quality analysis, Abaqus element quality checks found 32 elements that were distorted. It was shown that either the isoparametric angles were out of the suggested limits or the triangular or tetrahedral quality measure was bad. Table 5.2 shows the number of elements and nodes for each meshed model using the classical FE approach.

Table 5.1: Solution time for each classical FE case.

ClassicalFE model	**Total CPU time (sec)**
Keeled, centered load, not reamed	999.13
Keeled, centered load, reamed	1012.00
Keeled, eccentric superior load, reamed	1500.10
Keeled, centered load, reamed, with cement layer (mixture)	1069.10
Keeled, centered load, reamed, with cement layer (filled)	1000.60
Pegged, centered load, not reamed	1028.40
Pegged, centered load, reamed	973.47
Pegged, eccentric superior load, reamed	1014.90
Pegged, centered load, reamed, with cement layer (mixture)	1006.20
Pegged, centered load, reamed, with cement layer (filled)	968.34

Figures 5.2, 5.3 and 5.4 show the results for the keeled implant design qualitatively, Figures 5.5, 5.6 and 5.7 present the results for the pegged implant design and Figure 5.8 establishes a qualitative comparison between both implant designs. Data is also presented quantitatively using histograms (Figures 5.11, 5.12, 5.13, 5.14 and 5.10) that express von Mises stress values in regions with dimension of 4 mm in the y-direction, taken from the edge of the model, near the implant (Figure 5.1). For each region, the number of elements within a certain range of bone stress value is computed.

Table 5.2: Number of elements and nodes of the classical FE models.

ClassicalFE model	**Number of elements**	**Number of nodes**
Keeled, centered load, reamed	159153	29730
Keeled, centered load, reamed Keeled, eccentric superior load, reamed Keeled, centered load, reamed, with cement layer (mixture) Keeled, centered load, reamed, with cement layer (filled)	158004	29570
Pegged, centered load, not reamed	159523	29790
Pegged, centered load, reamed Pegged, eccentric superior load, reamed Pegged, centered load, reamed, with cement layer (mixture) Pegged, centered load, reamed, with cement layer (filled)	157923	29564

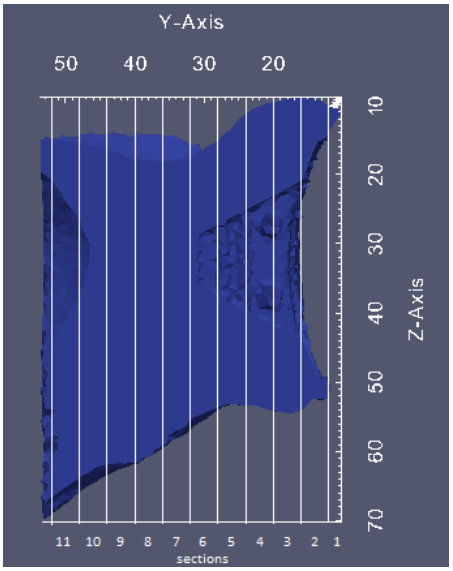

Figure 5.1: Representation of the 4 mm sections for which the results are presented in the histograms. Frontal anatomical cut of the glenoid region mesh with the keeled prosthetic component mesh subtracted.

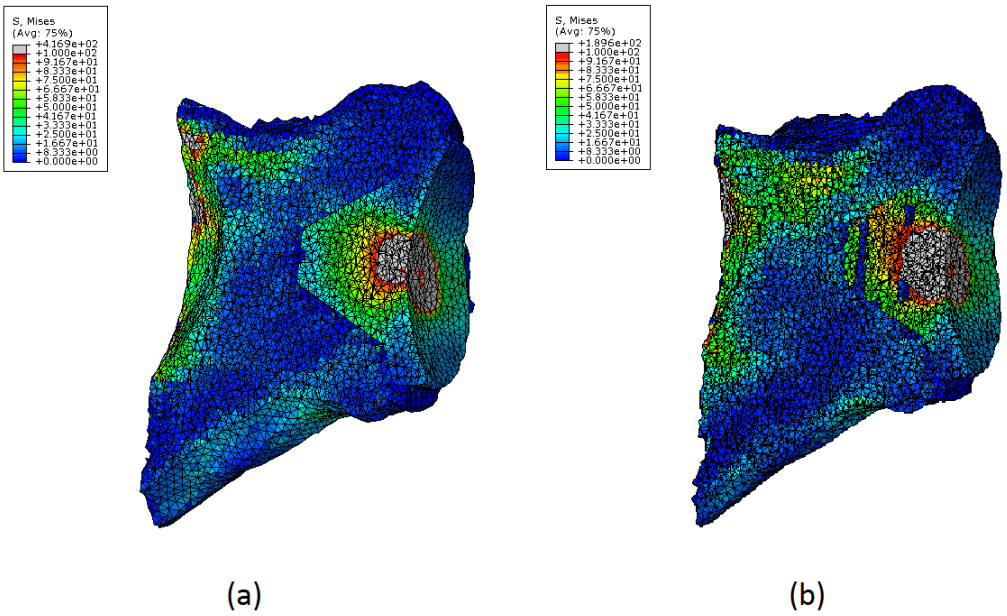

Figure 5.2: von Mises stress distribution resulting from centered compressive displacement of 1 mm for a keeled glenoid component: (a) without anatomic correction by bone ream of the glenoid surface and (b) with anatomic correction.

5.2 Micro-FE model: investigation of internal bone stresses

For the micro-FE approach two different factors were tested: one regarding the effect of implant design in stress distribution and another concerning loading position. The effect of implant design was modelled for a centered loading region, whereas the two different loading regions (centered and eccentric superior) were modelled for each design. Table 5.3 shows the solution time for each micro-FE simulated scenario and Table 5.4 shows the number of elements and nodes for each meshed model.

Table 5.3: Solution time for each micro-FE simulated case.

Micro-FE model	**Total CPU time (sec)**
Keeled, centered load	14945.8
Keeled, eccentric superior load	26680.5
Pegged, centered load	17342.8
Pegged, eccentric superior load	25795.4

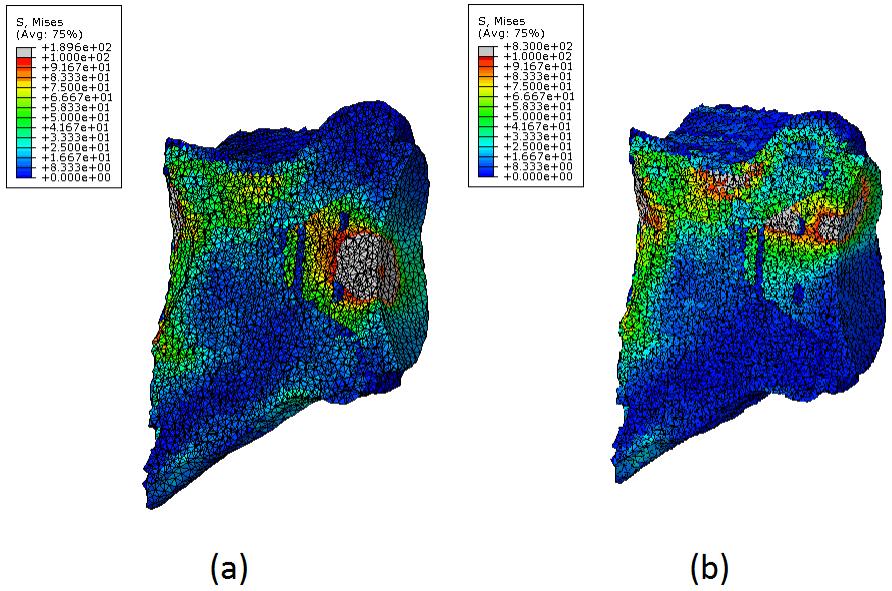

Figure 5.3: von Mises stress distribution resulting from a compressive displacement of 1 mm applied to a reamed glenoid surface with keeled glenoid component: (a) for a centered loading position and (b) for an eccentric superior loading position.

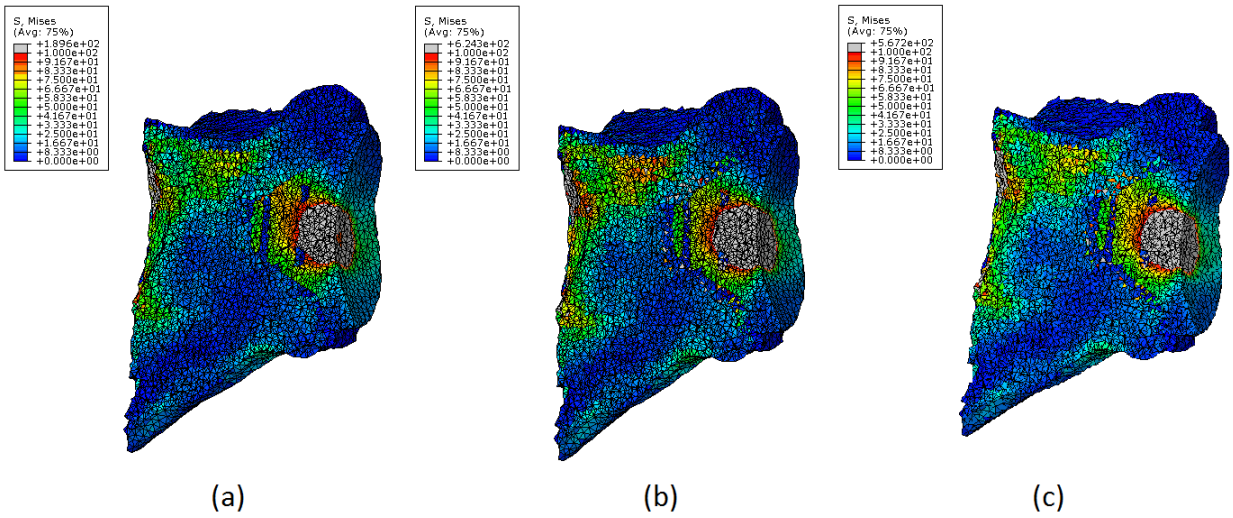

Figure 5.4: von Mises stress distribution resulting from centered compressive displacement of 1 mm applied to a reamed glenoid surface with keeled glenoid component and: (a) without cement layer, (b) with cement layer described by a rule of mixture, (c) with a cement layer completely filled.

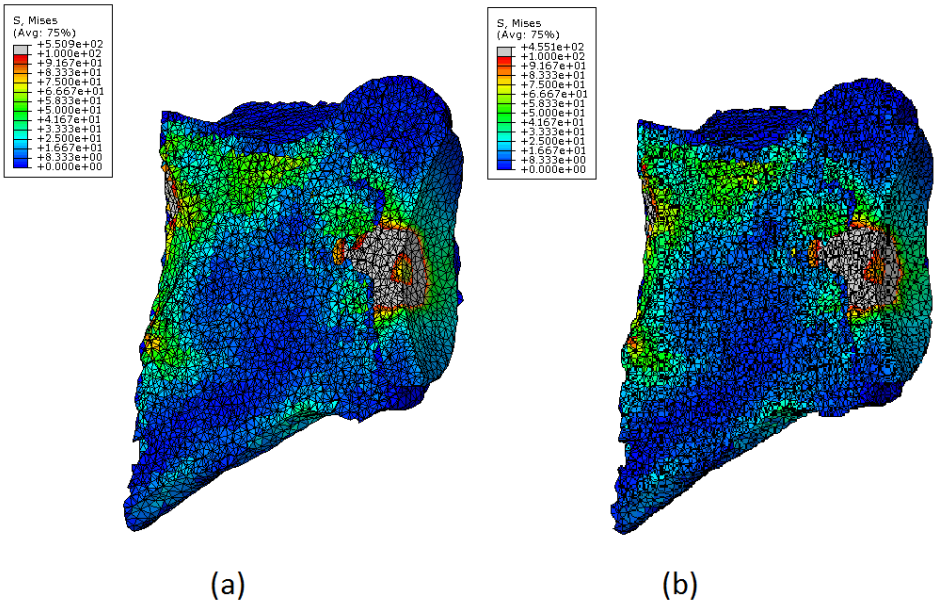

Figure 5.5: von Mises stress distribution resulting from centered compressive displacement of 1 mm for a pegged glenoid component: (a) without anatomic correction by bone ream of the glenoid surface and (b) with anatomic correction.

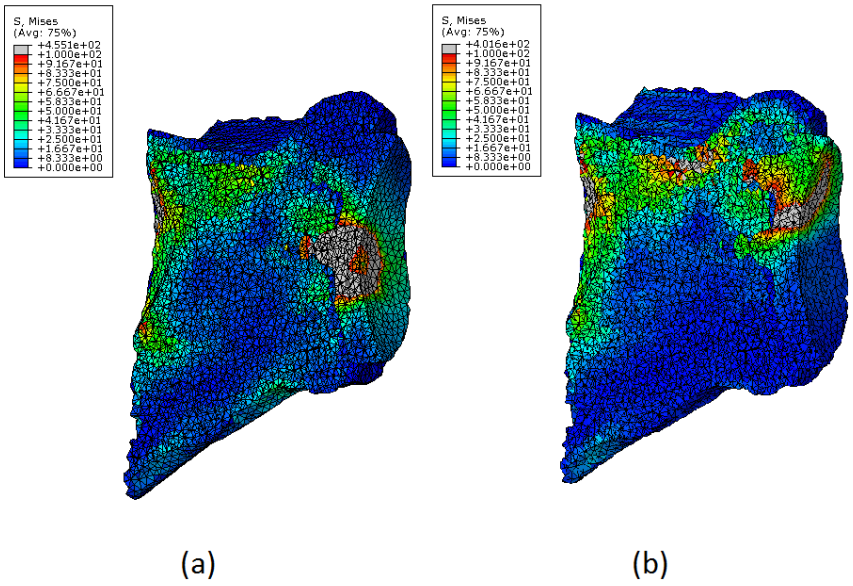

Figure 5.6: von Mises stress distribution resulting from a compressive displacement of 1 mm applied to a reamed glenoid surface with pegged glenoid component: (a) for a centered loading position and (b) for an eccentric superior loading position.

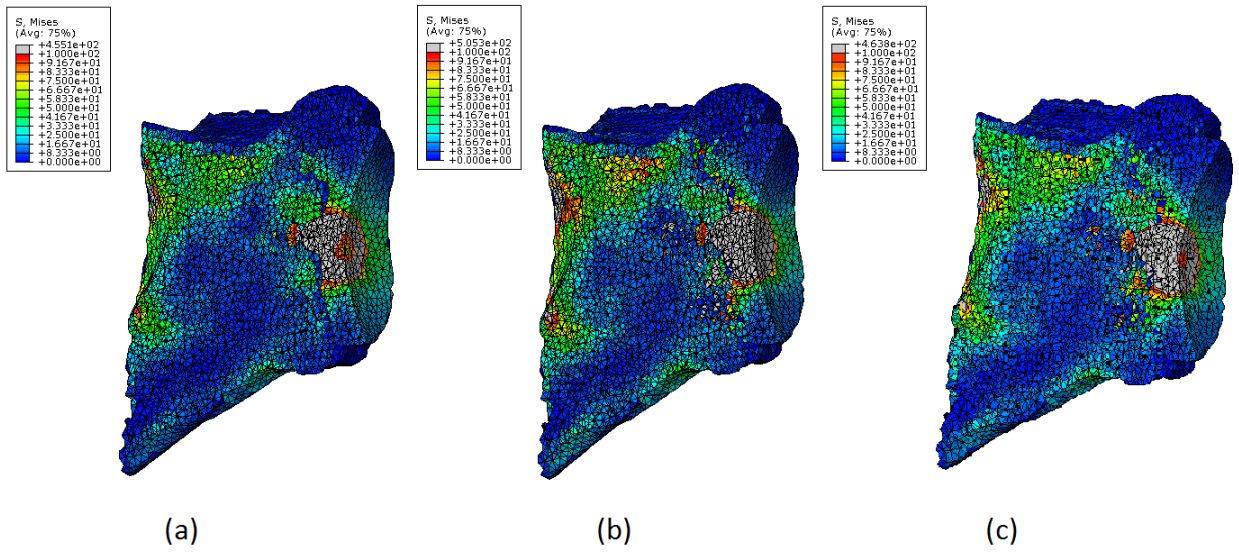

Figure 5.7: von Mises stress distribution resulting from centered compressive displacement of 1 mm applied to a reamed glenoid surface with pegged glenoid component and: (a) without cement layer, (b) with cement layer described by a rule of mixture, (c) with a cement layer completely filled.

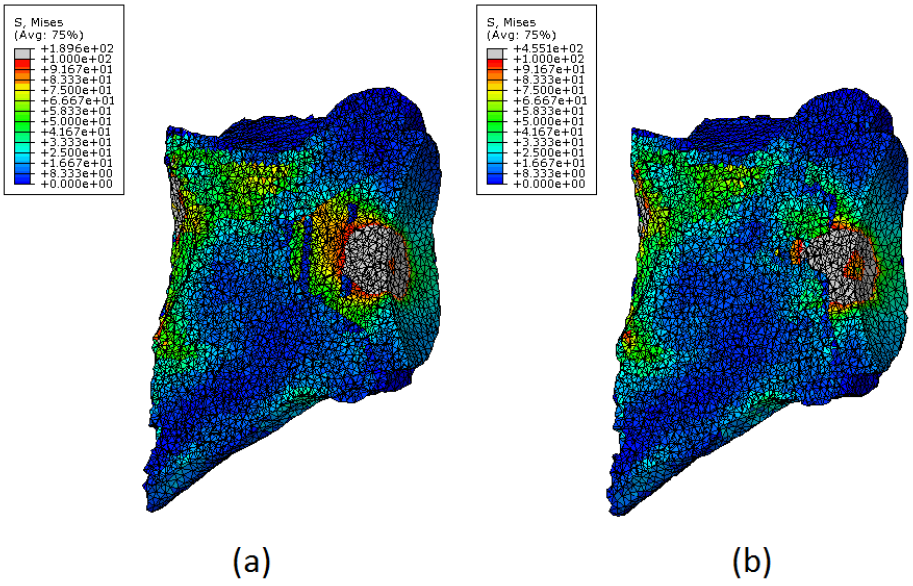

Figure 5.8: von Mises stress distribution resulting from centered compressive displacement of 1 mm applied to a reamed glenoid surface: (a) with keeled glenoid component (b) with pegged glenoid component.

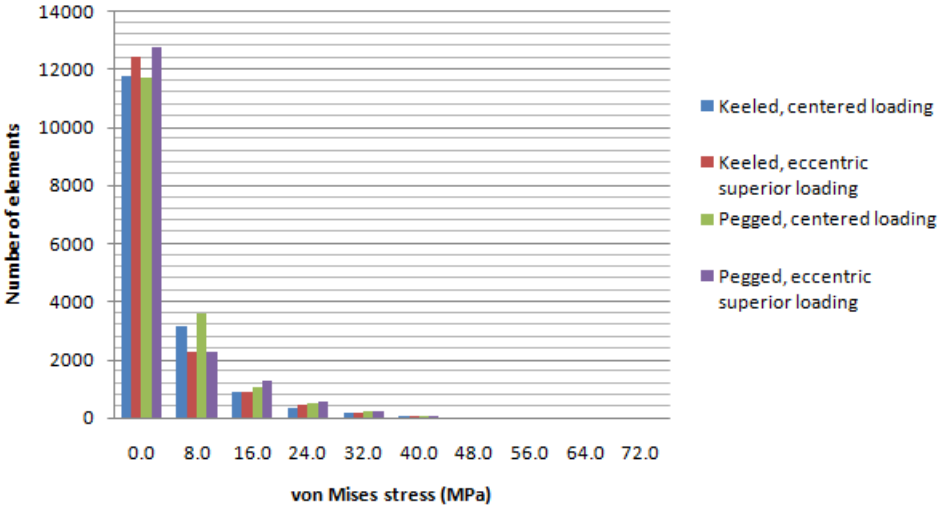

Figure 5.9: Histogram of the number of elements per range value of von Mises stress. Comparison between simulated loading positions for both keeled and pegged implant designs from a 12 mm to 16 mm region.

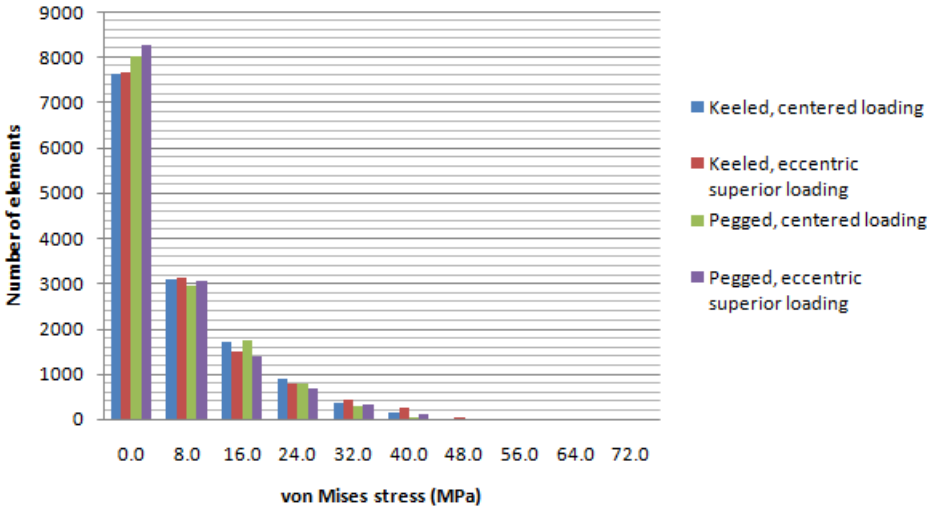

Figure 5.10: Histogram of the number of elements per range value of von Mises stress. Comparison between simulated loading positions for both keeled and pegged implant designs from a 28 mm to 32 mm region.

The simulations' results are presented in both qualitative (Figures 5.17, 5.15 and 5.16) and quantitative (Figures 5.18, 5.19, 5.20 and 5.21) data. The latter is presented in the form of histograms that express von Mises stresses in various regions with dimension of 50 voxels,

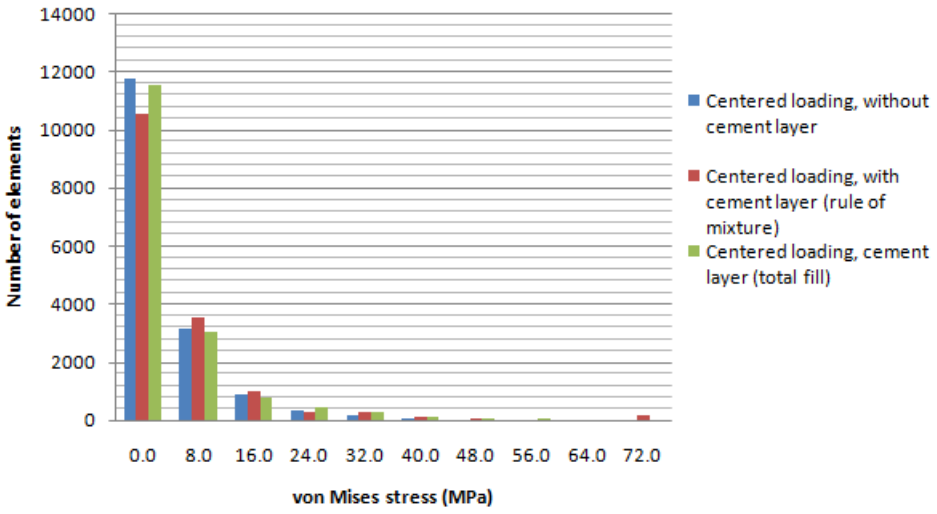

Figure 5.11: Histogram of the number of elements per range value of von Mises stress for the keeled implant design. Comparison between the cementless and cemented scenarios from a 12 mm to 16 mm region.

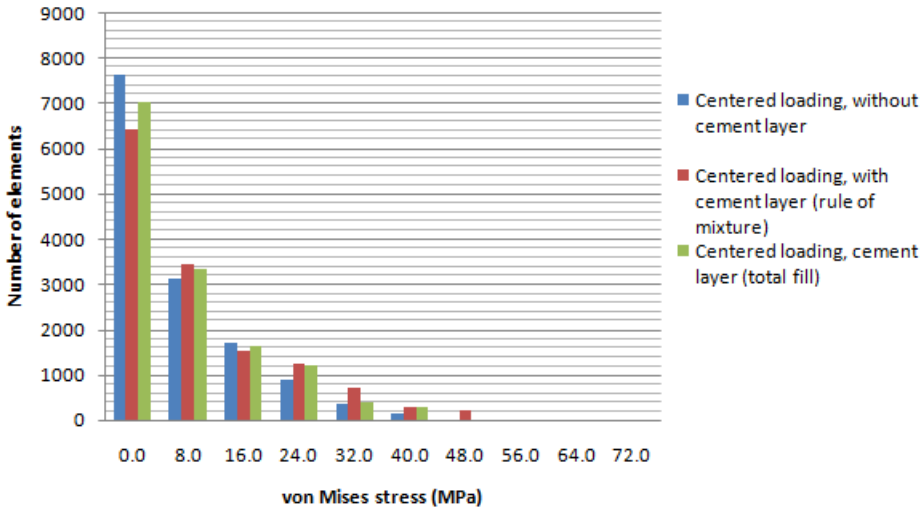

Figure 5.12: Histogram of the number of elements per range value of von Mises stress for the keeled implant design. Comparison between the cementless and cemented scenarios from a 28 mm to 32 mm region.

which corresponds to 4.1 mm slices in the y-direction, taken from the edge of the model. For each region, the histogram gives the number of elements within a certain range of bone stress values which were scaled to allow the comparison between the two numerical approaches.

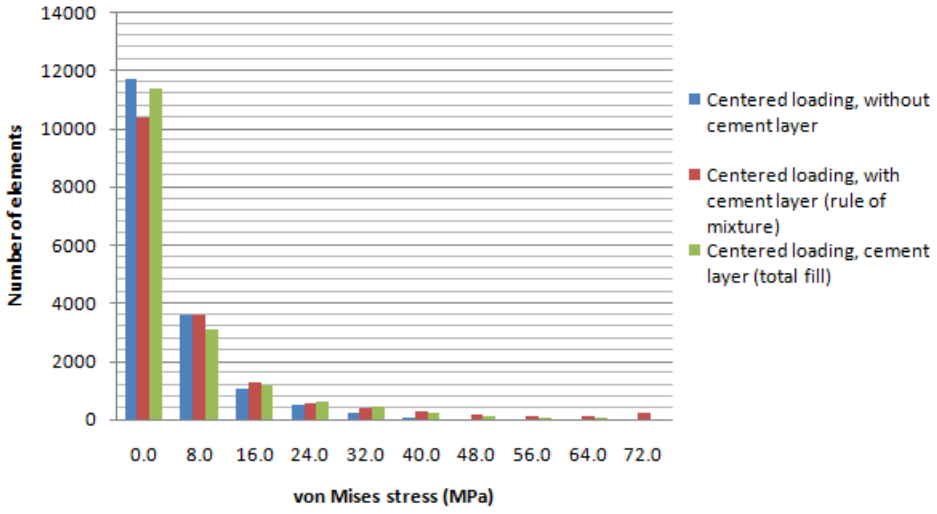

Figure 5.13: Histogram of the number of elements per range value of von Mises stress for the pegged implant design. Comparison between the cementless and cemented scenarios from a 12 mm to 16 mm region.

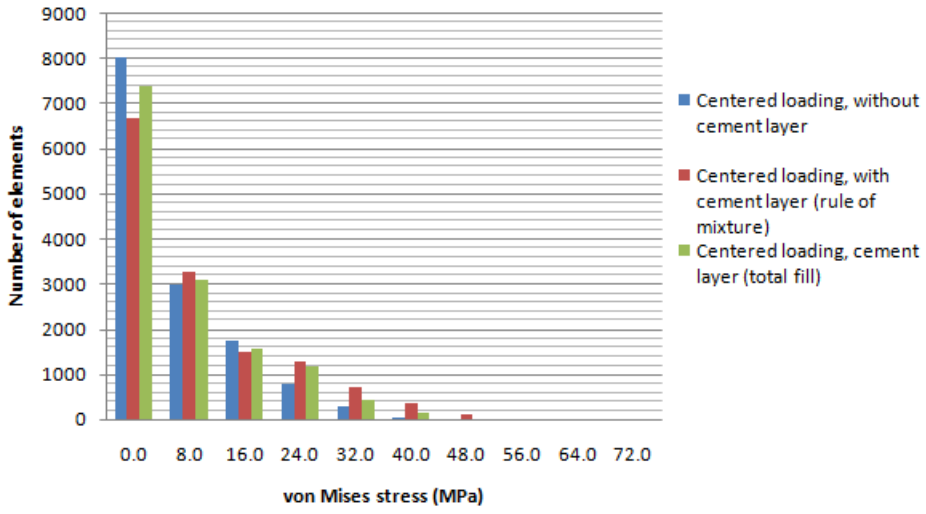

Figure 5.14: Histogram of the number of elements per range value of von Mises stress for the pegged implant design. Comparison between the cementless and cemented scenarios from a 28 mm to 32 mm region.

Table 5.4: Number of elements and nodes of the micro-FE models.

Micro-FE model	Number of elements	Number of nodes
Keeled, centered load Keeled, eccentric superior load	39995164	46972409
Pegged, centered load Pegged, eccentric superior load	39418615	46487047

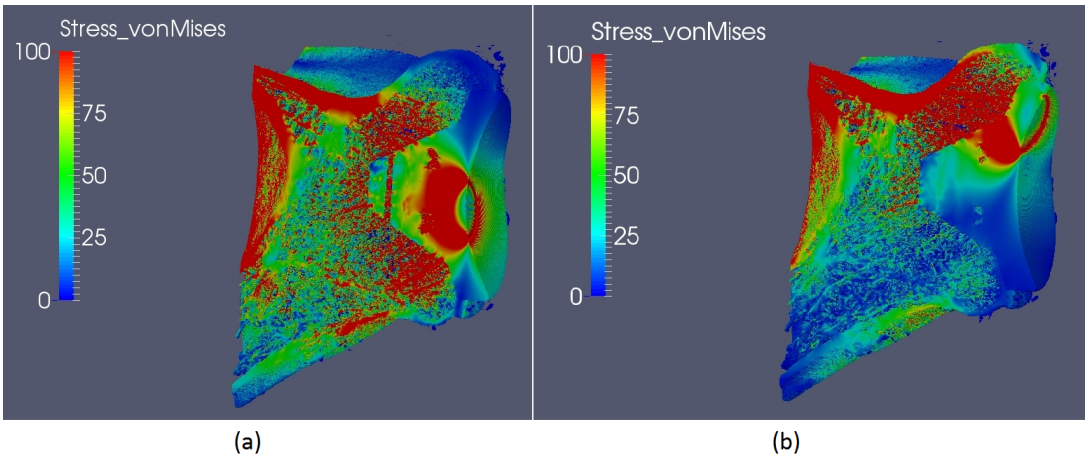

Figure 5.15: von Mises stress distribution for the keeled glenoid component, resulting from a compressive displacement of 1 mm applied at: (a) the centered loading position (b) the eccentric superior loading position.

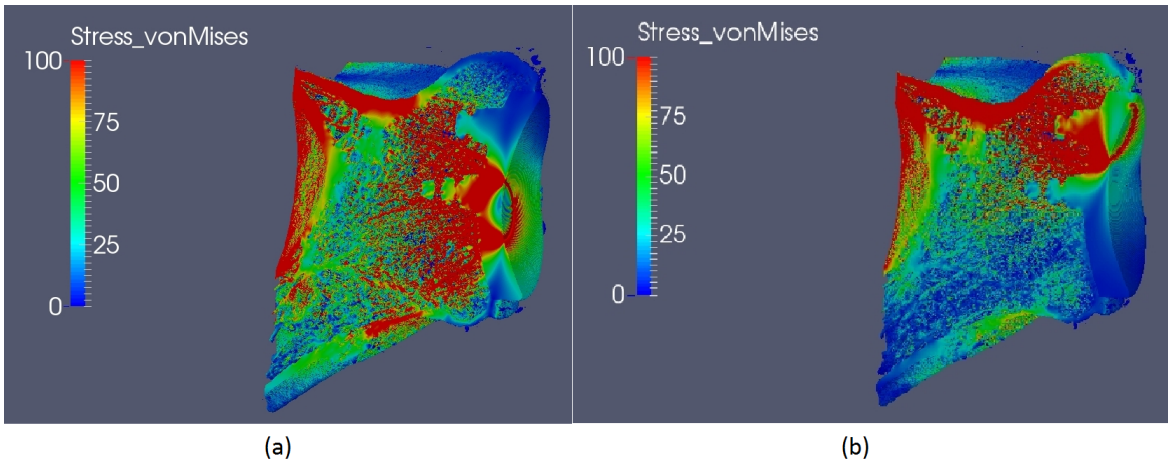

Figure 5.16: von Mises stress distribution for the pegged glenoid component, resulting from a compressive displacement of 1 mm applied at: (a) the centered loading position (b) the eccentric superior loading position.

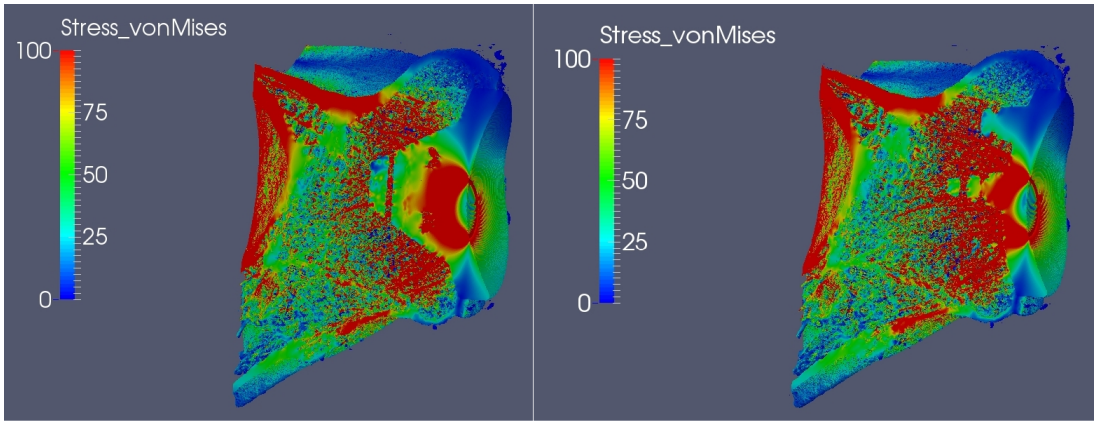

Figure 5.17: von Mises stress distribution resulting from a centered compressive displacement of 1 mm: (a) for the keeled glenoid component, (b) for the pegged glenoid component.

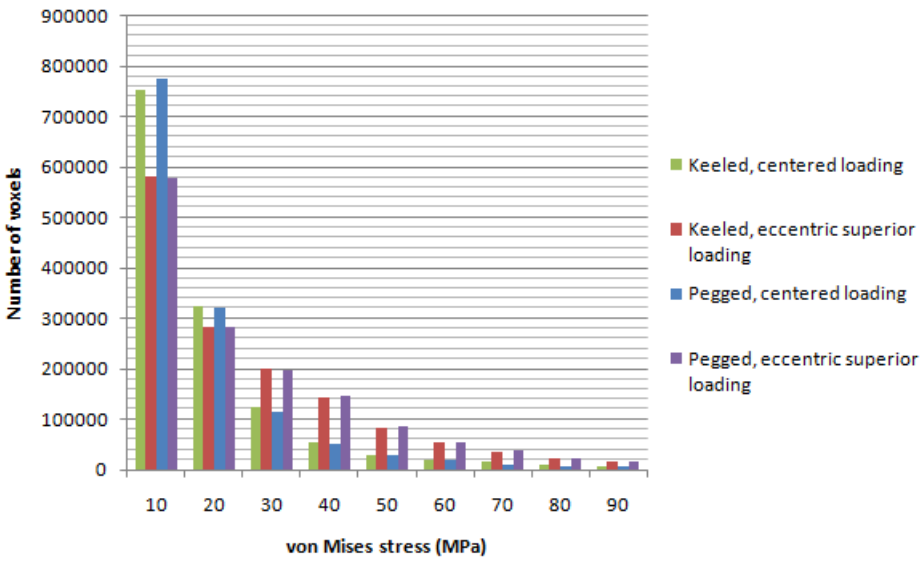

Figure 5.18: Histogram of the number of voxels per range value of von Mises stress. Comparison between simulated cases from a 12.3 mm to 16.4 mm region.

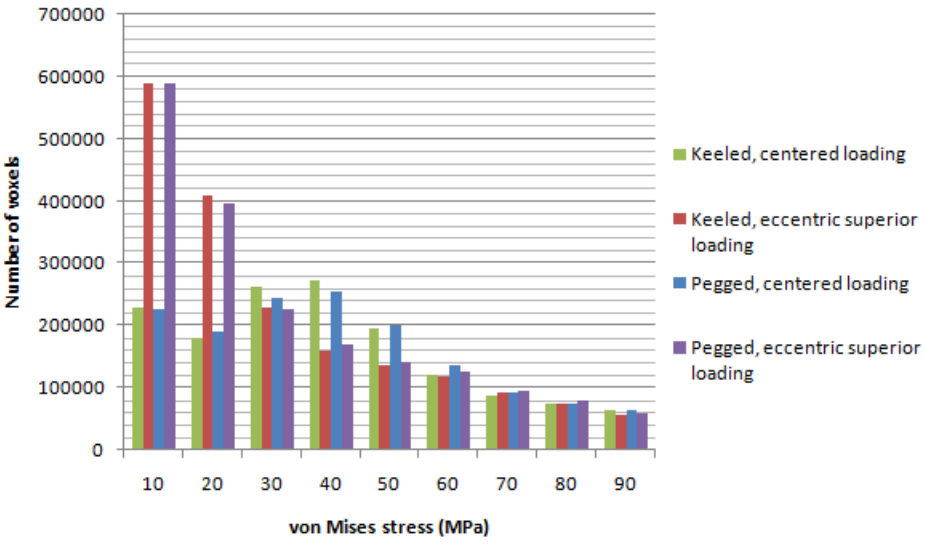

Figure 5.19: Histogram of the number of voxels per range value of von Mises stress. Comparison between simulated cases from a 20.5 mm to 24.6 mm region.

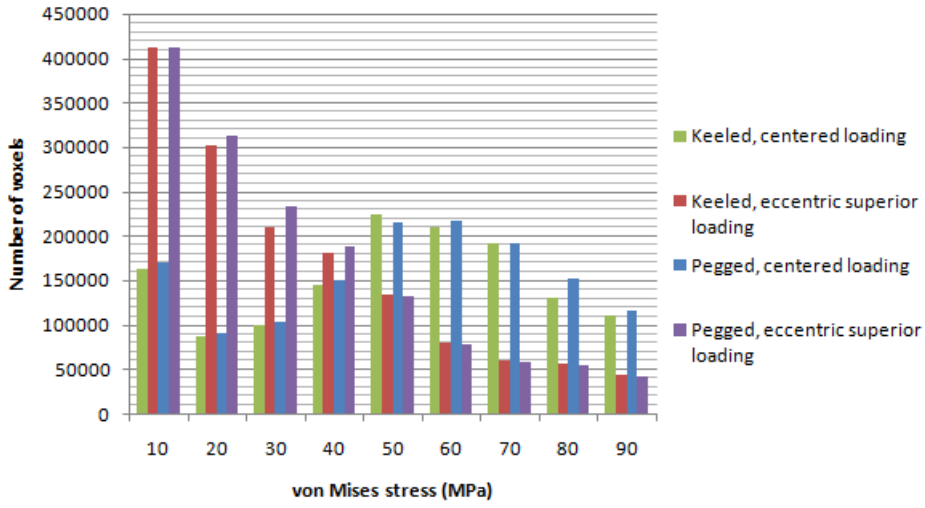

Figure 5.20: Histogram of the number of voxels per range value of von Mises stress. Comparison between simulated cases from a 28.7 mm to 32.8 mm region.

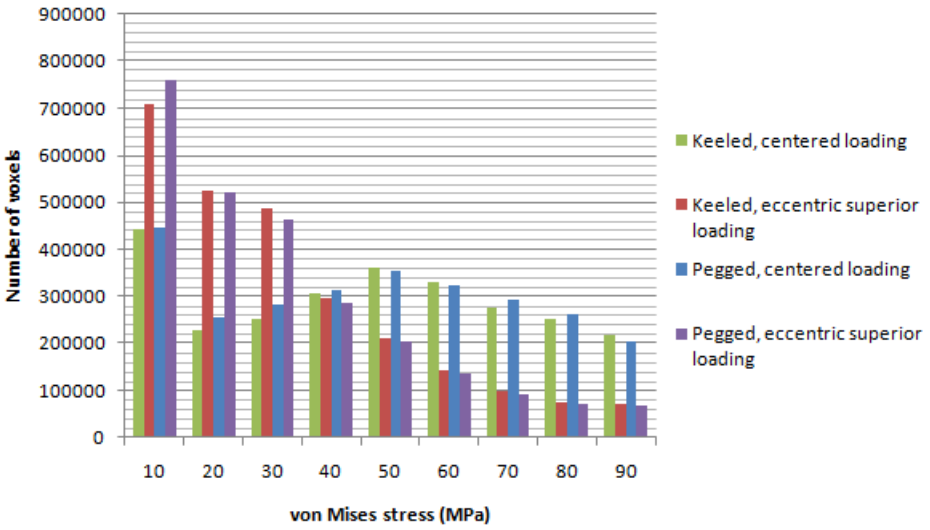

Figure 5.21: Histogram of the number of voxels per range value of von Mises stress. Comparison between simulated cases from a 32.8 mm to 36.9 mm region.

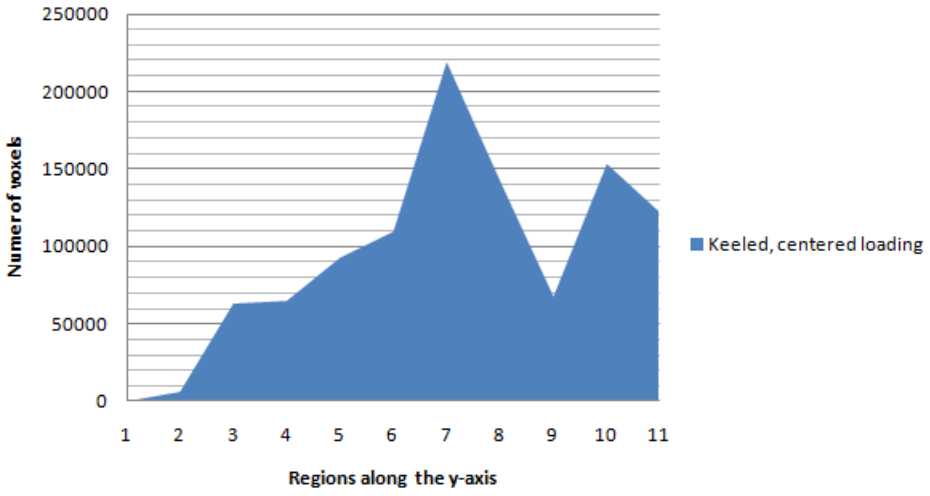

Figure 5.22: Distribution of a von Mises stress of 90 MPa along the different bone regions defined as 4 mm sections.

Chapter 6

Discussion

The introduction of a glenoid implant alters significantly the load transfer pattern in the glenoid. Without a prosthetic component, the joint load is initially transferred to the underlying cancellous bone and then gradually to the cortical bone coating the scapular body. Previous studies (Patel et al., 2014) showed that the insertion of a glenoid implant results in a load redistribution so that the implant and cement carry a considerable amount of load.

6.1 Classical FE model

The histograms are presented for four different regions that were chosen accordingly to the proximity of the implant. The objective was to analyse the stress distribution in the bone-implant interface. Therefore, the von Mises stress is computed for regions 2 and 6. Regions 9, 10 and 11 were not considered in any analysis because the results near this edge of the bone model were influenced by the assumed boundary conditions (fully constrained in all directions), resulting in the increase of von Mises stress.

The first research question dealt with was the influence of a bone ream. It was observed, for the keeled design, that anatomic glenoid correction affected more the bone closer to the implant, were higher stresses were registered (Figure 5.2). Glenoid anatomic correction is

important to provide better glenoid component fixation, but in this case the bone ream was particularly beneficial in obtaining a more refined mesh. Considering the pegged design, the bone ream did not seem to affect the stress distribution (Figure 5.5).

Out second research question dealt with the influence of implant design. The results (Figure 5.8) show that cancellous bone undergoes more compressive stress with the pegged design than with the keeled one. Stresses seem to be better distributed away from the glenoid surface with the keeled design. However, these differences are better observed with the micro-FE model, since the trabecular geometry is taken into account.

Our third research question concerned the effect of changing the applied load position. For both glenoid component designs, stress distribution and loading position were congruent, with a larger amount of stress affecting the upper area of the glenoid during eccentric superior loading (Figures 5.3 and 5.6). Quantitatively (Figures 5.9 and 5.10), higher stress values were observed closer to the glenoid surface in eccentric loading. The observed compressive stress on the superior side and tensile stress on the inferior side of the glenoid confirm the "rocking horse" phenomenon, suggesting that glenoid loosening is likely to occur with eccentric loading.

The fourth research question dealt with the effect of adding a cement layer and changing its properties. In the case where no cement layer was added, the stresses were largely supported by the implant and then transferred to the bone, mainly compact bone in the case of the keeled design (Figure 5.4), and more cancellous bone in the case of the pegged design (Figure 5.7). When cement is added to the pegs and keel, the latter become stiffer than the surrounding bone and, as a result, carry the load normally carried by the cancellous bone in an intact glenoid. Adding cement also increases the fixation of the implant, however, the rigidity of the implant-bone system also increases, originating higher stresses around this interface (Figure 5.11 and 5.13). Thus, regarding the cement layer described as a rule of mixture, higher stresses were observed near the glenoid surface, but also farther from the end of the keel and pegs (Figure 5.12 and 5.14). On the other hand, the cement layer described as totally filled by cement showed lower stresses in both the selected regions, with a stress

distribution similar to the cement layer described by the rule of mixture. It is expected that the regions of the cement mantle that are supported by trabecular bone are more likely to undergo larger deformations and result in larger stresses, increasing the risk of cement fracture.

6.2 Micro-FE model

Concerning the loading location, for both keeled and pegged designs (Figures 5.15 and 5.16), the observed concentration of compressive stresses on the superior side of the glenoid corroborates the "rocking-horse" phenomenon, with a great amount of load being transferred to that cancellous bone region whereas lower stresses reach the inferior glenoid area. This is also shown trough the histograms (Figures 5.19, 5.19, 5.20 and 5.21) where a higher amount of stress is located closer to the glenoid surface: more voxels registered values of 90 MPa of von Mises stress when compared with results for centered loading.

Regarding the differences between keeled and pegged designs (Figure 5.17), the results suggest that the implant design influences the stress distribution, as seen also with the classical FE model. We can observe that the keeled design spreads the stresses more away from the glenoid surface, than the pegged design. Once the keel occupies a larger area than the pegs and goes deeper into bone, load carried in the cancellous bone was bypassed to the distal cortical bone. Longer pegs would possibly allow load to be transferred to the cancellous bone later, increasing the likelihood for stress shielding by decreasing stress in near glenoid surface. The histograms corroborate this tendency, with higher values of von Mises stress being registered for the pegged design. Though there are not great quantitative differences, it is possible to observe qualitatively that the keeled design causes the load to bypass the cancellous bone, which decreases stress in the bone, thus decreasing bone resorption.

Figure 5.22 shows the number of voxels that registered a value of von Mises stress above 90 MPa, along the different defined regions, for the keeled glenoid design and a centrally applied load. We can observe that near the glenoid surface and bone-implant interface the

number of voxels that registered this amount of stress is lower, growing continuously as the distance to the glenoid surface increases. The peak occurs at region 7, which corresponds to a distance of 32 mm to 36 mm from the glenoid surface, away from the end of the keel. However, it is clear that, for both implant designs, stresses are mainly distributed along the bone-implant interface, where bone remodelling would occur. Changes in internal loads, resulting in lower or higher stresses would affect this interface, acting as a trigger for bone resorption or damage.

Chapter 7

Conclusions and Outlook

The main objective of this thesis was to investigate how internal loads in the bone are affected by different implantation scenarios regarding the design of the implant, loading conditions and cementing technique. The results were analysed and compared both qualitatively and quantitatively.

The results obtained in this thesis can be used to interpret the effects of design of the shoulder glenoid components on the induced stresses at the bone-cement and bone-implant interface. By using refined micro-FE models of implanted glenoids, this study provided a new methodology that allows an accurate prediction of the internal bone tissue stresses distribution in the glenoid, after TSA. The results from the micro-FE approach were congruent with the results obtained with the classical approach.

The micro-FE approach has shown to be useful to evaluate more accurately how internal bone tissue is affected by design changes in the prosthetized shoulder. It provided a better modelling of bone structures that include the effects of trabecular network, revealing how the different scenarios can influence bone stresses and how these could lead to bone remodelling and potential loosening of the implant.

Regarding the quality of the elements, first-order triangular and tetrahedral elements, like the C3D4 used in these models, are often avoided in stress analysis problems due to their higher stiffness and slow convergence with mesh refinement. To obtain results of suffi-

cient accuracy usually an extremely fine mesh is needed. However, tetrahedral elements are geometrically versatile and provided a more accurate geometrical representation of the bone structure and implant. Although a few elements have been considered distorted during the analyses in Abaqus, it did not influence negatively the overall results.

Because this study was based on one bone, the results should be interpreted in terms of the general effects of implant design, loading location and cementing technique. Anatomic variables vary from individual to individual, however, the purpose of this study was not to predict specific stresses in a particular person or for a daily activity, and therefore, comparison of these results must be interpreted accordingly.

Furthermore, our study lacks an experimental validation component. The results, nonetheless, are in good agreement with previous experimental and computer simulation studies.

To sum up, my work involved developing a reliable methodology that combined both classical and micro-FE approaches and testing it for different glenoid component designs. For each design, different loading positions, anatomical correction and cementing techniques were studied. In the micro-FE approach only the effect of loading position for each glenoid prosthesis was tested. Besides, I also designed a positioning setup for the scapula that will be used in the experimental validation.

Future work involves investigating the influence of bone quality and conformity on the stability of the glenoid component for designs of anatomical and reversed replacement, such as metal backing and hybrid designs. This implies testing these models with more specimens and validating with experimental data. Testing other implant positions and degrees of glenoid correction will also help understanding the bone-implant system and contribute to improve TSA surgery outcomes.

References

Anglin, C., Tolhurst, P., Wyss, U. P., & Pichora, D. R. (1999). Glenoid cancellous bone strength and modulus. *Journal of Biomechanics*, *32*, 1091–1097.

Armstrong, A., & Lewis, G. (2013). Design evolution of the glenoid component in total shoulder arthroplasty. *Journal of Bone and Joint Surgery*, *1*(2).

Beck, J. D., Canfield, B. L., Haddock, S. M., Chen, T. J., Kothari, M., & Keaveny, T. M. (1997, Sep). Three-dimensional imaging of trabecular bone using the computer numerically controlled milling technique. *Bone*, *21*(3), 281–287.

Bohsali, K., Wirth, M., & Rockwood, C. J. (Oct 2006). Complications of total shoulder arthroplasty. *J Bone Joint Surg Am*, *88*(10), 2279–2292.

Boileau, P., Avidor, C., Krishnan, S., Walch, G., Kempf, J., & Molé, D. (2002). Cemented polyethylene versus uncemented metal-backed glenoid components in total shoulder arthroplasty: a prospective, double-blind, randomized study. *J Shoulder Elbow Surg*, *11*(4), 351–359.

Brems, J. (1993). The glenoid component in total shoulder arthroplasty. *J Shoulder Elbow Surg*, 247–254.

Burr, D. B., Forwood, M. R., Fyhrie, D. P., Martin, R. B., Schaffler, M. B., & Turner, C. H. (1997). Bone microdamage and skeletal fragility in osteoporotic and stress fractures. *J Bone Miner Res*, *12*(1), 6–15.

Burr, D. B., Martin, R., Schaffler, M. B., & Radin, E. L. (1985). Bone remodeling in response to in vivo fatigue microdamage. *Journal of Biomechanics*, *18*(3), 189 - 200.

Chalmers, P. N., Gupta, A. K., Rahman, Z., Bruce, B., Romeo, A. A., & Nicholson, G. P. (April 2004). Predictors of early complications of total shoulder arthroplasty. *The Journal of Arthroplasty*, *29*(4), 856–860.

Chevalier, Y. (2008). *Computer tomography-based finite element analysis of the human vertebral body.* Unpublished doctoral dissertation, Fakultät für Maschinenwesen und Betriebswissenschaften,Technischen Universität Wien.

Chevalier, Y., Pahr, D., Allmer, H., Charlebois, M., & Zysset, P. (2007). Validation of a voxel-based FE method for prediction of the uniaxial apparent modulus of human trabecular bone using macroscopic mechanical tests and nanoindentation. *Journal of Biomechanics*, *40*(15), 3333–3340.

Chevalier, Y., Pahr, D., & Zysset, P. (2009). The role of cortical shell and trabecular fabric in finite element analysis of the human vertebral body. *J Biomech Eng*, *131*(11).

Couteau, B., Mansat, P., Estivalézes, E., Darmana, R., Mansat, M., & Egan, J. (2001). Finite

element analysis of the mechanical behavior of a scapula implanted with a glenoid prosthesis. *Clin Biomech*, *16*(7), 566–575.

Currey, J. D. (1988). The effect of porosity and mineral content on the young's modulus of elasticity of compact bone. *J Biomech*, *21*(2), 131–139.

Franklin, J., Barrett, W., Jackins, S., & Matsen, F. (1988). Glenoid loosening in total shoulder arthroplasty. association with rotator cuff deficiency. *J Arthroplasty*, *3*(1), 39–46.

Frich, L. H., Jensen, N. C., Odgaard, A., Pedersen, C. M., Sobjberg, J. O., & Dalstra, M. (1997). Bone strength and material properties of the glenoid. *Journal of Shoulder and Elbow Surgery*, *6*, 97–104.

Friedman, R. J., LaBerge, M., Dooley, R. L., & OHara, A. L. (1992). Finite element modeling of the glenoid component: Effect of design parameters on stress distribution. *J Shoulder Elbow Surg*, *1*, 261–270.

Gartsman, G., Elkousy, H., Warnock, K., Edwards, T., & O Connor, D. (May 2005). Radiographic comparison of pegged and keeled glenoid components. *J Shoulder Elbow Surg*, *14*(3), 252-257.

Gere, J. M. (2004). *Mechanics of materials* (T. Brooks/Cole, Ed.). Bill Stenquist.

Gupta, S., van der Helm, F., & van Keulen, F. (2004). Stress analysis of cemented glenoid prostheses in total shoulder arthroplasty. *Journal of Biomechanics*, *37*, 177–1786.

Gupta, S., & van der Helm, F. C. (2004). Load transfer across the scapula during humeral abduction. *Journal of Biomechanics*, *37*, 1001–1009.

Hattrup, S., & Cofield, R. (2009). Osteonecrosis of the humeral head: results of replacement. *J Shoulder Elbow Surg*, *9*(3), 177–182.

Hayes, W. C., & Carter, D. R. (Jul 1976). Postyield behavior of subchondral trabecular bone. *J Biomed Mater Res*, *10*(4), 537–544.

Hengsberger, S., Kulik, A., & Zysset, P. (Jan 2001). A combined atomic force microscopy and nanoindentation technique to investigate the elastic properties of bone structural units. *Eur Cell Mater*, *1*, 12–17.

Hernandez, C. J., Beaupré, G. S., Keller, T. S., & Carter, D. R. (2001). The influence of bone volume fraction and ash fraction on bone strength and modulus. *Bone*, *29*(1), 74–78.

Hibbeler, R. C. (2008). *Mechanics of materials* (7th ed.). Person Prentice Hall.

Hopkins, A. R., Hansen, U. N., Amis, A. A., & Emery, R. (2004). The effects of glenoid component alignment variations on cement mantle stresses in total shoulder arthroplasty. *J Shoulder Elbow Surg*, *13*, 668–675.

Ibarra, C., Dines, D. M., & McLaughlin, J. A. (Jul 1998). Glenoid replacement in total shoulder arthroplasty. *Orthopedic Clinics of North America*, *29*(3).

Kabel, J., van Rietbergen, B., Odgaard, A., & Huiskes, R. (Oct 1999). Constitutive relationships of fabric, density, and elastic properties in cancellous bone architecture. *Bone*, *25*(4), 481–486.

Keaveny, T. M., Guo, X. E., Wachtel, E. F., McMahon, T. A., & Hayes, W. C. (Sep 1994). Trabecular bone exhibits fully linear elastic behavior and yields at low strains.

J Biomech, *27*(9), 1127–1136.

Keaveny, T. M., Morgan, E. F., Niebur, G. L., & Yeh, O. C. (2001). Biomechanics of trabecular bone. *Annu Rev Biomed Eng*, *3*, 307–333.

Kinney, J. H., Lane, N. E., & Haupt, D. L. (1995, Feb). In vivo, three-dimensional microscopy of trabecular bone. *J Bone Miner Res*, *10*(2), 264–270.

Kosmopoulos, V., & Keller, T. S. (Nov 2004). Damage-based finite-element vertebroplasty simulations. *Eur Spine J*, *13*(7), 617–625.

Kotha, S. P., & Guzelsu, N. (Dec 2003). Effect of bone mineral content on the tensile properties of cortical bone: experiments and theory. *J Biomech Eng*, *125*(6), 785–793.

Kuhn, J. L., Goldstein, S. A., Feldkamp, L. A., Goulet, R. W., & Jesion, G. (1990, Nov). Evaluation of a microcomputed tomography system to study trabecular bone structure. *J Orthop Res*, *8*(6), 833–842.

Kutz, M. (2002). *Standard handbook of biomedical engineering and design* (1st ed.). McGraw-Hill.

Lacroix, D., Murphy, L., & Prendergast, P. (2000). Three-dimensional finite element analysis of glenoid replacement prostheses: a comparison of keeled and pegged anchorage systems. *J Biomech Eng.*, *122*(4), 430–436.

Lacroix, D., & Prendergast, P. (1997). Stress analysis of glenoid component designs for shoulder arthroplasty. *Proc Instn Mech Engrs*, *211*(H).

Lazarus, M., Jensen, K., Southworth, C., & Matsen, F. (2002). The radiographic evaluation of keeled and pegged glenoid component insertion. *J Bone Joint Surg Am*, *84*(7), 1174–1182.

Matsuura, M., Eckstein, F., Lochmüller, E.-M., & Zysset, P. K. (Feb 2008). The role of fabric in the quasi-static compressive mechanical properties of human trabecular bone from various anatomical locations. *Biomech Model Mechanobiol*, *7*(1), 27–42.

Mazza, G., Franzoso, G., Pretterklieber, M., & Zysset, P. (2008). Anisotropic elastic properties of vertebral compact bone measured by microindentation. *In European Society of Biomechanics, Luzern, Switzerland,*.

Moreno, R., Borga, M., & Smedby, r. (2012). Generalizing the mean intercept length tensor for gray-level images. *Medical physics*, *39*(7), 4599–4612.

Neer, C., Watson, K., & Stanton, F. (Mar 1982). Recent experience in total shoulder replacement. *J Bone Joint Surg Am*, *64*(3), 319–337.

Odgaard, A. (1997, Apr). Three-dimensional methods for quantification of cancellous bone architecture. *Bone*, *20*(4), 315–328.

Pahr, D., Dall'Ara, E., Varga, P., & Zysset, P. (2012). HR-pQCT-based homogenised finite element models provide quantitative predictions of experimental vertebral body stiffness and strength with the same accuracy as micro-FE models. *Comput Methods Biomech Biomed Engin.*, *15*(7), 711–720.

Patel, R. J., Wright, T. M., & Gao, Y. (2014). Load transfer after cemented total shoulder arthroplasty. *J Shoulder Elbow Surg*, *23*(10), 1553–1562.

Rüegsegger, P., Koller, B., & Müller, R. (Jan 1996). A microtomographic system for the

nondestructive evaluation of bone architecture. *Calcif Tissue Int*, *58*(1), 24–29.

Röhl, L., Larsen, E., Linde, F., Odgaard, A., & Jorgensen, J. (1991). Tensile and compressive properties of cancellous bone. *J Biomech*, *24*(12), 1143–1149.

Rho, J. Y., Tsui, T. Y., & Pharr, G. M. (Oct 1997). Elastic properties of human cortical and trabecular lamellar bone measured by nanoindentation. *Biomaterials*, *18*(20), 1325–1330.

Roy, M. E., Rho, J. Y., Tsui, T. Y., Evans, N. D., & Pharr, G. M. (Feb 1999). Mechanical and morphological variation of the human lumbar vertebral cortical and trabecular bone. *J Biomed Mater Res*, *44*(2), 191–197.

Sanchez-Sotelo, J. (Mar 2011). Total shoulder arthroplasty. *Open Orthop J.*, *16*(5), 106–114.

Seeley, R., Stephens, T., & Tate, P. (2007). *Anatomy and physiology*. McGraw-Hill.

Sperling, J., Cofield, R., & Rowland, C. (2004). Minimum fifteen-year follow-up of neer hemiarthroplasty and total shoulder arthroplasty in patients aged fifty years or younger. *J Shoulder Elbow Surg*, *13*(6), 604-613.

Strang, G., & Fix, G. (1973). *An analysis of the finite element method*. Prentice Hall.

Suárez, D. R., Nerkens, W., Valstar, E. R., Rozing, P. M., & van Keulen, F. (Apr 2012). Interface micromotions increase with less-conforming cementless glenoid components. *J Shoulder Elbow Surg.*, *21*(4), 474–482.

Terrier, A., Büchler, P., & Farron, A. (2005). Bone-cement interface of the glenoid component: stress analysis for varying cement thickness. *Clinical Biomechanics*, *20*, 710–717.

Terrier, A., Büchler, P., & Farron, A. (2006). Influence of glenohumeral conformity on glenoid stresses after total shoulder arthroplasty. *J Shoulder Elbow Surg*.

Van Buskirk, W. C., Cowin, S. C., & Ward, R. N. (May 1981). Ultrasonic measurement of orthotropic elastic constants of bovine femoral bone. *J Biomech Eng*, *103*(2), 67–72.

van Rietbergen, B., Weinans, H., Huiskes, R., & Odgaard, A. (1995, Jan). A new method to determine trabecular bone elastic properties and loading using micromechanical finite-element models. *J Biomech*, *28*(1), 69–81.

Wainwright, S., Gosline, J., & Biggs, W. (1976). *Mechanical design in organisms*. New York: Halsted Press.

Wang, X., Bank, R. A., TeKoppele, J. M., & Agrawal, C. M. (2001). The role of collagen in determining bone mechanical properties. *Journal of Orthopaedic Research*, *19*(6), 1021–1026.

Westerhoff, P., Graichen, F., Bender, A., Halder, A., Beier, A., Rohlmann, A., & Bergmann, G. (2009). In vivo measurement of shoulder joint loads during activities of daily living. *J Biomech*, *42*(12), 1840–1849.

Whitehouse, W. J. (Jul 1974). The quantitative morphology of anisotropic trabecular bone. *J Microsc*, *101*(Pt 2), 153–168.

Wirth, M., & Rockwood, C. (1996). Complications of total shoulderreplacement arthroplasty. *J Bone Joint Surg Am*, *78*, 603–616.

Yongpravat, C., Kim, H. M., Gardner, T. R., Bigliani, L. U., Levine, W. N., & Ahmad, C. S. (2013). Glenoid implant orientation and cement failure in total shoulder arthroplasty: a finite element analysis. *J Shoulder Elbow Surg*, *22*, 940–947.

Zhang, J., Yongpravat, C., Kim, H. M., Levine, W. N., Bigliani, L. U., Gardner, T. R., & Ahmad, C. S. (Mar 2013). Glenoid articular conformity affects stress distributions in total shoulder arthroplasty. *J Shoulder Elbow Surg.*, *22*(3), 350–356.

Zysset, P. K., Guo, X. E., Hoffler, C. E., Moore, K. E., & Goldstein, S. A. (Oct 1999). Elastic modulus and hardness of cortical and trabecular bone lamellae measured by nanoindentation in the human femur. *J Biomech*, *32*(10), 1005-1012.

Zysset, P. K., Sonny, M., & Hayes, W. C. (Apr 1994). Morphology-mechanical property relations in trabecular bone of the osteoarthritic proximal tibia. *J Arthroplasty*, *9*(2), 203–216.

Appendices

Appendix A

CAD drawings

In this chapter the CAD drawings of the positioning setup that were sent to the workshop of Klinikum Grosshadern are presented. The first drawing corresponds to the assembly of all components and the second one to the assembly of only the cylinder and its base plate. The latter was constructed with two different materials: aluminium, to assemble then in the remaining parts of the final setup, and PVC to assist only in the specimens' embedding (Figure A.1). This PVC cylinder design was adapted to its function, being higher (80 mm instead of 60 mm) and not divided in two pieces as the one made of aluminium and shown in the drawing. The remaining drawings correspond to the parts that support the structure and allow the tilting of the scapula placed in the cylinder, being still in construction.

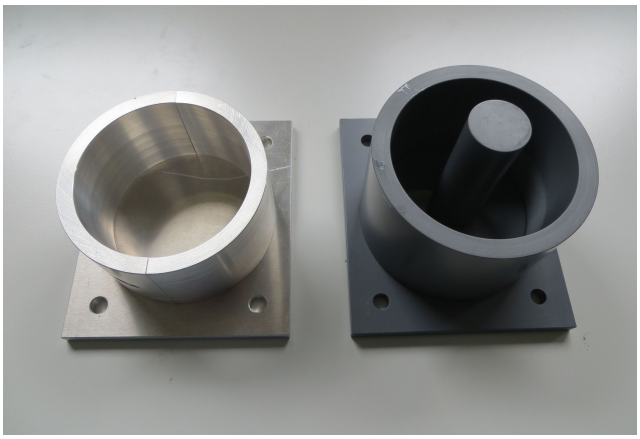

Figure A.1: Top part of the setup: cylinder and base plate made of aluminium (left) and PVC (right).

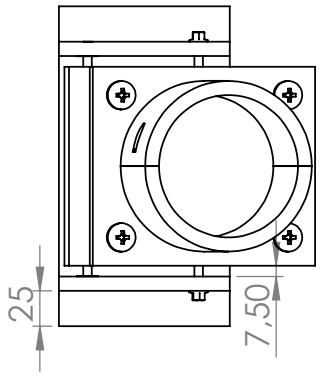

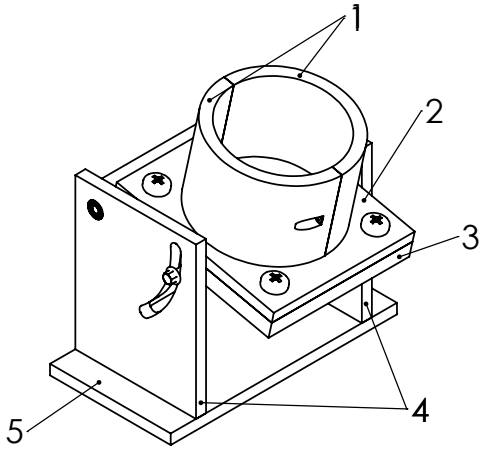

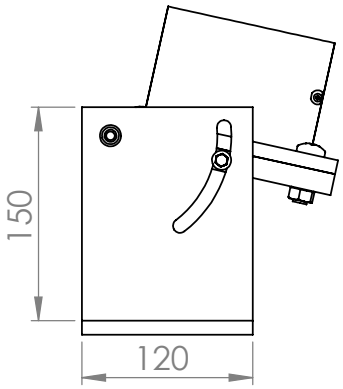

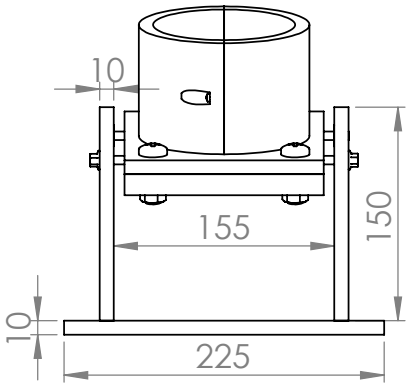

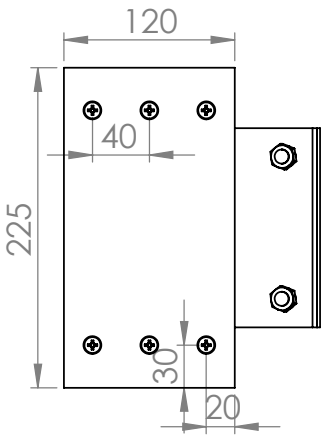

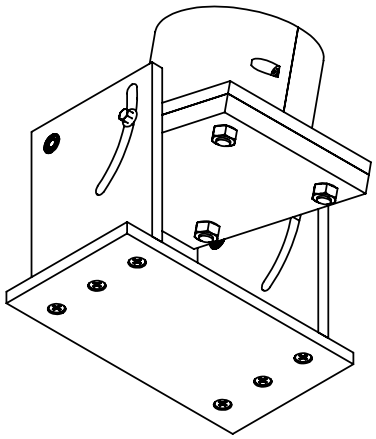

DIMENSIONS ARE IN MILLIMETRES						DO NOT SCALE DRAWING	REVISION
						Labor für Biomechanik und Experimentalle Orthopädie	
	NAME	SIGNATURE	DATE			TITLE: Positioning setup for scapula	
DRAWN	Inês Santos		02-05-2014				
CHK'D							
APPV'D							
MFG							
Q.A				MATERIAL: Aluminum		DWG NO. Final	A4
				WEIGHT:		SCALE: 1: 3	SHEET 1 OF 1

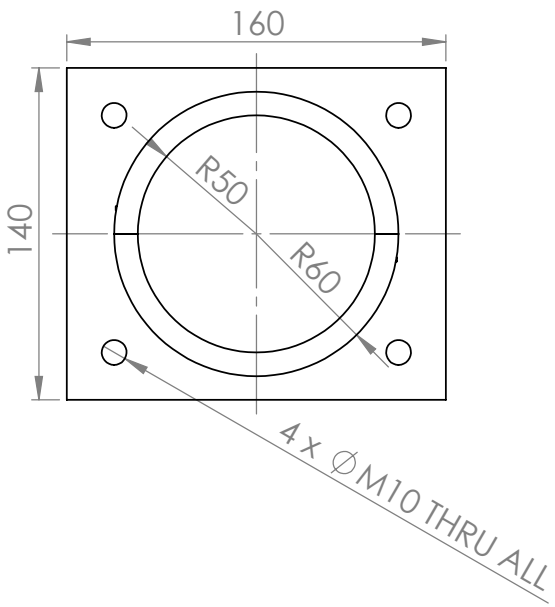

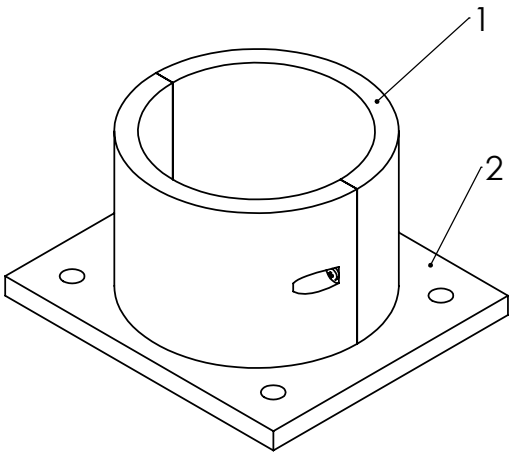

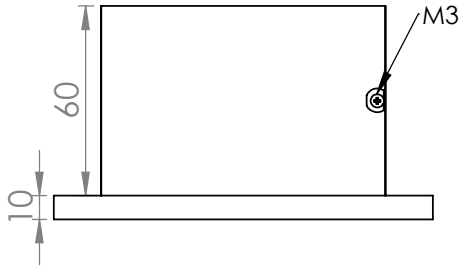

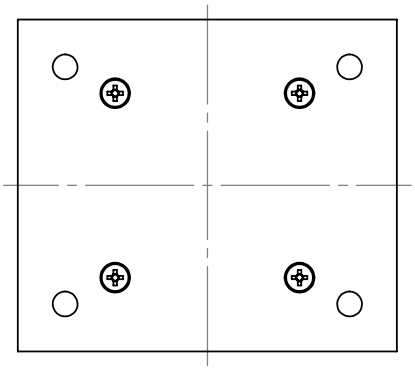

DIMENSIONS ARE IN MILLIMETRES					DO NOT SCALE DRAWING	REVISION
					Labor für Biomechanik und Experimentalle Orthopädie	
	NAME	SIGNATURE	DATE		TITLE:	
DRAWN	Inês Santos		05-05-2014		Positioning setup for scapula	
CHK'D						
APPV'D						
MFG						
Q.A				MATERIAL: Aluminum	DWG NO. Cylinder + Base plate	A4
				WEIGHT:	SCALE: 1: 3	SHEET 1 OF 1

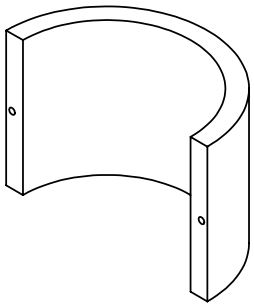

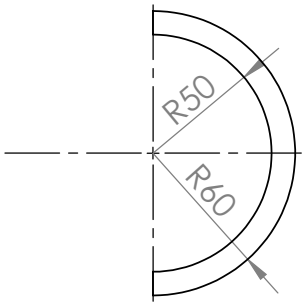

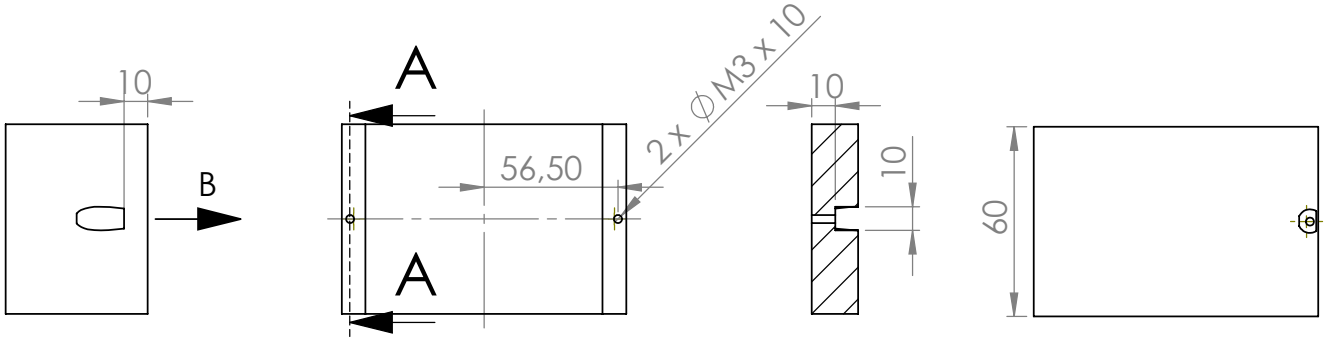

VIEW B

SECTION A-A

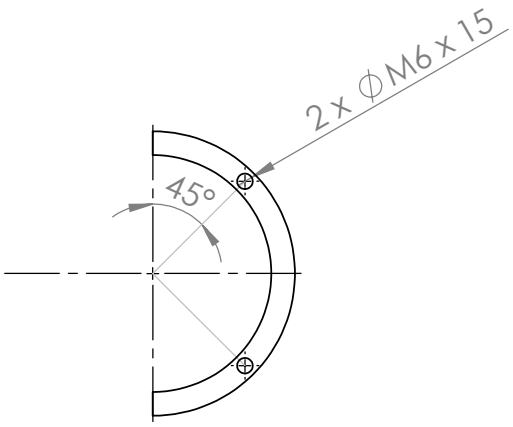

DIMENSIONS ARE IN MILLIMETRES	2 Pieces			DO NOT SCALE DRAWING	REVISION	
				Labor für Biomechanik und Experimentalle Orthopädie		
	NAME	SIGNATURE	DATE	TITLE: Positioning setup for scapula		
DRAWN	Inês Santos		05-05-2014			
CHK'D						
APPV'D						
MFG						
Q.A				MATERIAL: Aluminum	DWG NO. 1. Cylinder	A4
				WEIGHT:	SCALE: 1: 2	SHEET 1 OF 1

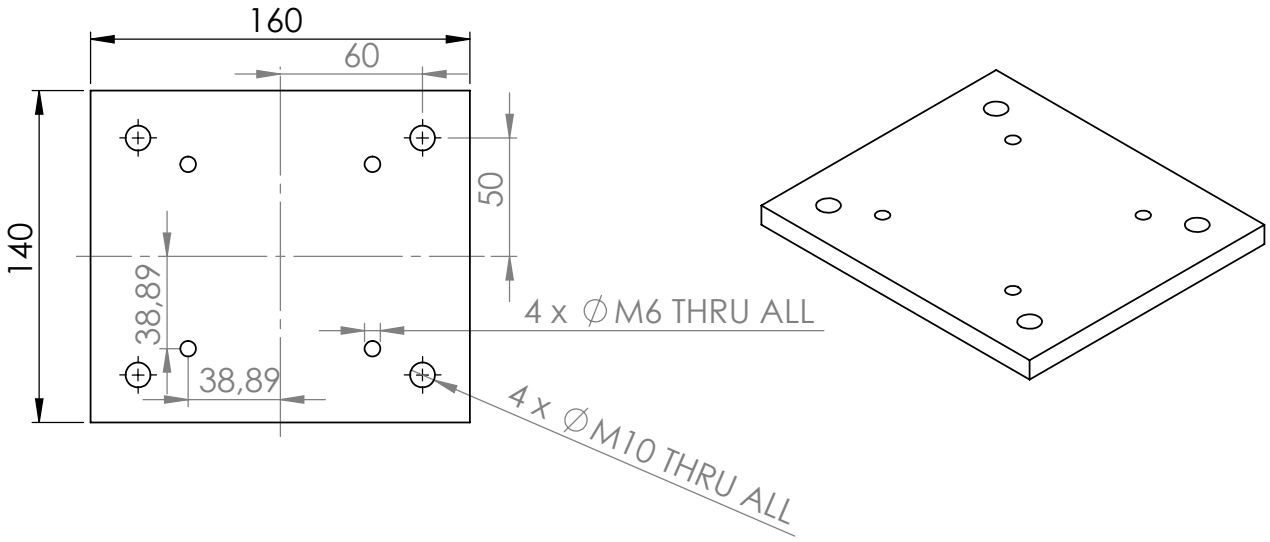

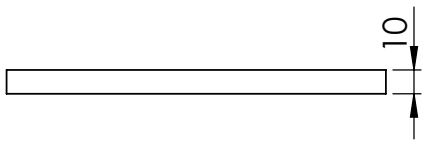

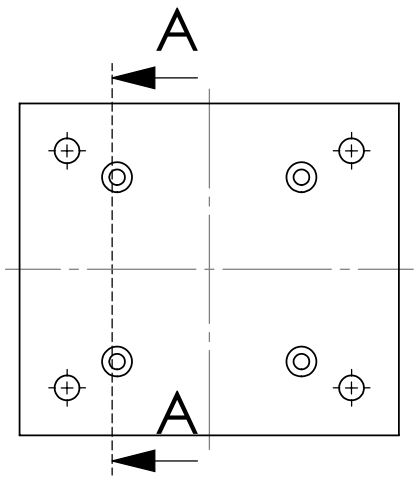

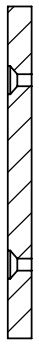

SECTION A-A

DIMENSIONS ARE IN MILLIMETRES	1 Piece				DO NOT SCALE DRAWING	REVISION
					Labor für Biomechanik und Experimentalle Orthopädie	
	NAME	SIGNATURE	DATE		TITLE:	
DRAWN	Inês Santos		02-05-2014		Positioning setup for scapula	
CHK'D						
APPV'D						
MFG						
Q.A				MATERIAL: Aluminum	DWG NO. 2. Cylinder's base plate	A4
				WEIGHT:	SCALE: 1: 3	SHEET 1 OF 1

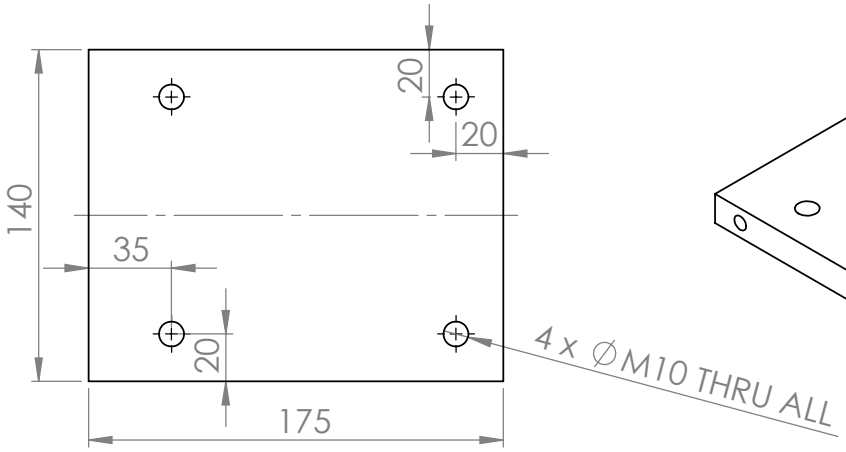

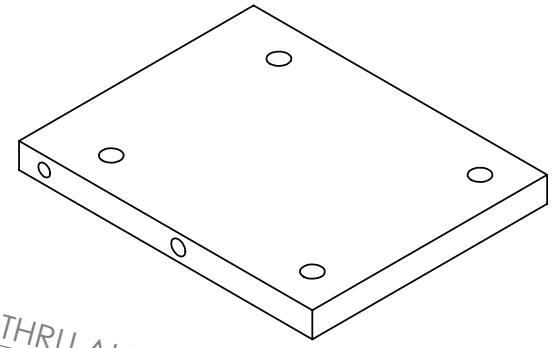

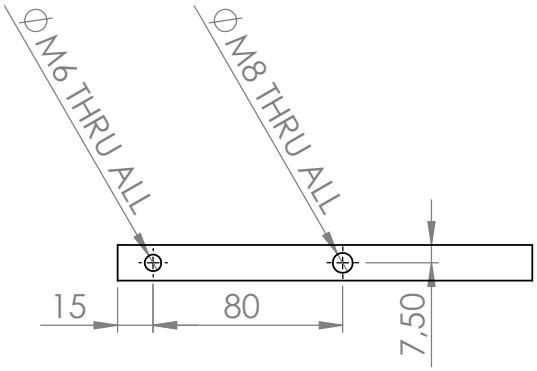

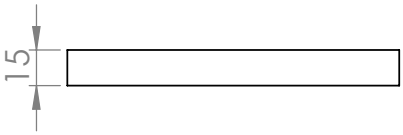

DIMENSIONS ARE IN MILLIMETRES		1 Piece			DO NOT SCALE DRAWING	REVISION
					Labor für Biomechanik und Experimentalle Orthopädie	
	NAME	SIGNATURE	DATE		TITLE:	
DRAWN	Inês Santos		02-05-2014		Positioning setup for scapula	
CHK'D						
APPV'D						
MFG						
Q.A				MATERIAL:	DWG NO.	A4
				Aluminum	3. Rotating plate	
				WEIGHT:	SCALE: 1: 3	SHEET 1 OF 1

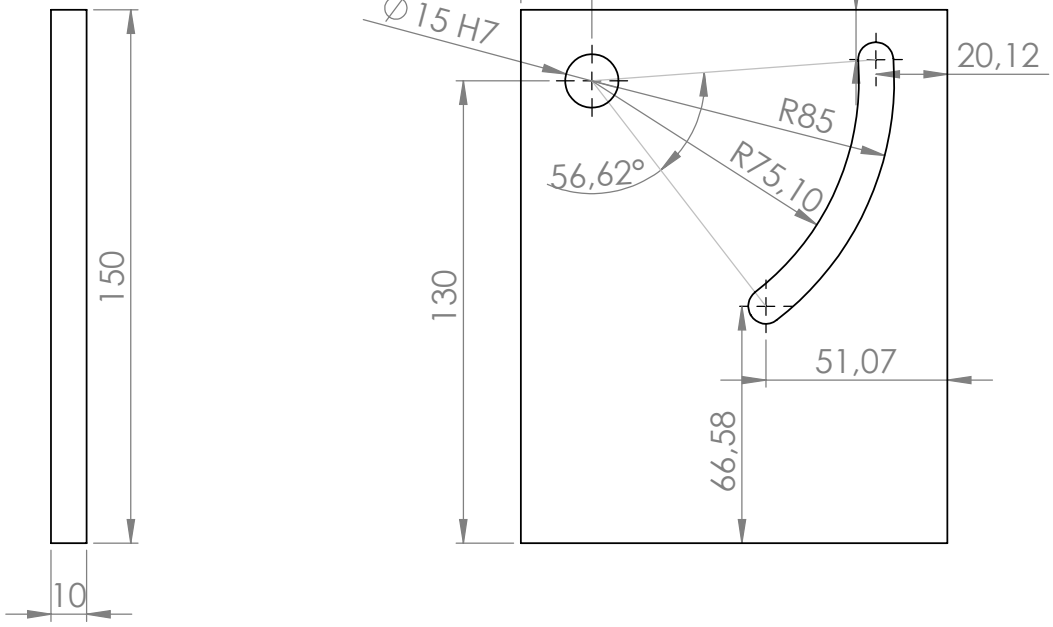

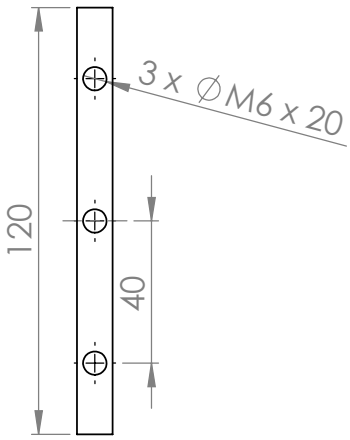

DIMENSIONS ARE IN MILLIMETRES		2 Pieces				DO NOT SCALE DRAWING	REVISION
						Labor für Biomechanik und Experimentalle Orthopädie	
	NAME	SIGNATURE	DATE			TITLE:	
DRAWN	Inês Santos		02-05-2014			Positioning setup for scapula	
CHK'D							
APPV'D							
MFG							
Q.A				MATERIAL:		DWG NO.	A4
				Aluminum		4. Lateral plate	
				WEIGHT:		SCALE: 1: 2	SHEET 1 OF 1

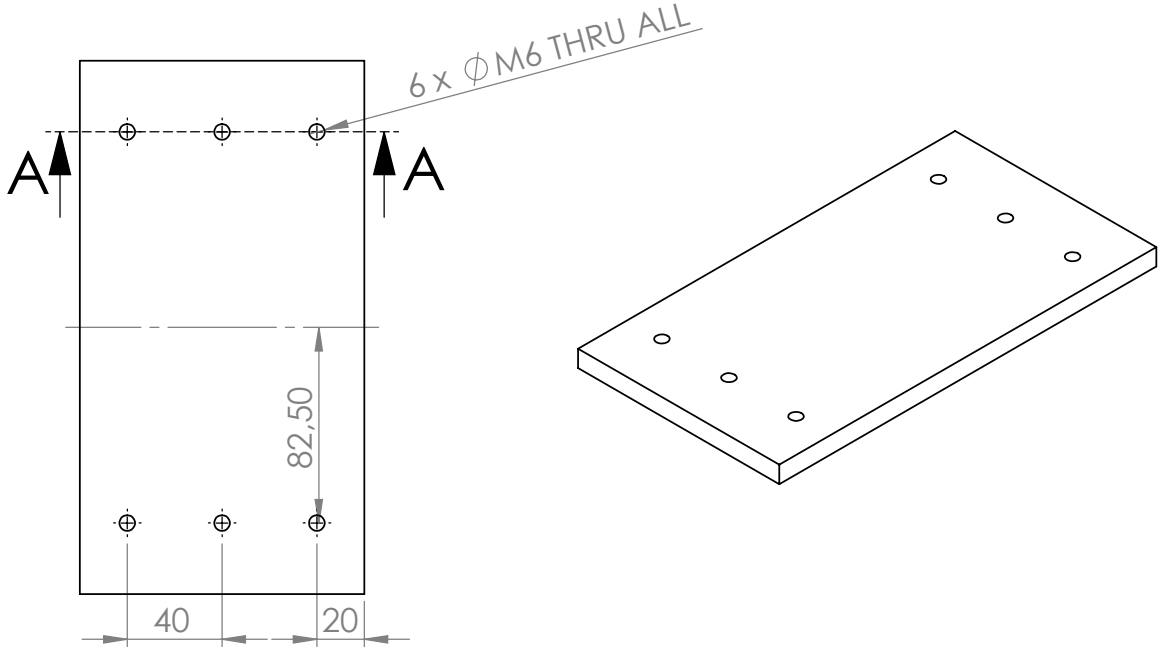

SECTION A-A

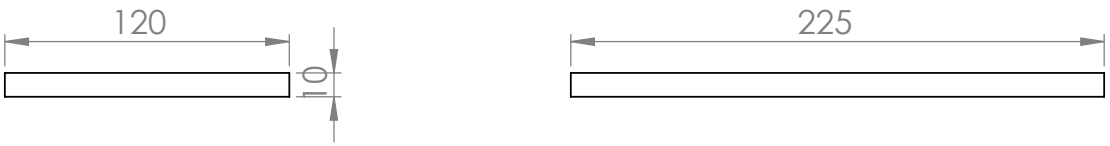

DIMENSIONS ARE IN MILLIMETRES		1 Piece				DO NOT SCALE DRAWING	REVISION
						Labor für Biomechanik und Experimentalle Orthopädie	
	NAME	SIGNATURE	DATE			TITLE:	
DRAWN	Inês Santos		02-05-2014			Positioning setup for scapula	
CHK'D							
APPV'D							
MFG							
Q.A				MATERIAL:		DWG NO.	A4
				Aluminum		5. Base	
				WEIGHT:		SCALE: 1: 3	SHEET 1 OF 1

Appendix B

Mechanics of materials

In this chapter some fundamental physical quantities considered important to understand bone mechanics are defined.

Normal and shear stress - Normal stress is the intensity of the force acting normal to a small area ΔA, that is, arising from the force vector component perpendicular to the material cross section on which it acts. If the normal force or stress "pulls" on ΔA it is referred to as tensile stress, whereas if it "pushes" on ΔA it is called compressive stress. On the other hand, shear stress is defined as the component of stress coplanar with a material cross section (Hibbeler, 2008).

The dimension of stress is that of pressure, and therefore its coordinates are commonly measured in the same units as pressure: pascals (Pa or N/m^2 or $m^{-1}.kg.s^{-2}$).

Strain - The concept of strain describes the deformation of a body by changes in length of line segments and the changes in the angles between them (Hibbeler, 2008).

Poisson's ratio - This physical quantity is the negative ratio of transverse to axial strain. When a material is compressed in one direction it usually tends to expand in the other two directions perpendicular to the direction of compression. This phenomenon is

called the Poisson effect, being the Poisson's ratio ν its measure. Thus, the Poisson's ratio is the fraction (or percent) of expansion divided by the fraction (or percent) of compression, for small values of these changes.

The Poisson's ratio of a stable, isotropic, linear elastic material cannot be less than 1.0 nor greater than 0.5 due to the requirement that Young's modulus, the shear modulus and bulk modulus have positive values. Most materials have Poisson's ratio values ranging between 0.0 and 0.5. A perfectly incompressible material deformed elastically at small strains would have a Poisson's ratio of exactly 0.5 (Gere, 2004).

Young's modulus - Also known as the tensile modulus or elastic modulus, it is a measure of the stiffness of an elastic material. It is defined as the ratio of the stress (force per unit area) along an axis to the strain (ratio of deformation over initial length) along that axis in the range of stress in which Hooke's law holds (Gere, 2004).

Young's modulus is the most common elastic modulus, sometimes called the modulus of elasticity, but there are other elastic moduli measured, such as the bulk modulus and the shear modulus. Once stress has units of pressure and strain is dimensionless, the unit of Young's modulus is pascal(Pa or N/m^2 or $m^{-1}.kg.s^{-2}$).

von Mises yield criterion - In materials science and engineering this criterion can be formulated in terms of the von Mises stress or equivalent tensile stress, σ_v, a scalar stress value that can be computed from the Cauchy stress tensor. In this case, a material is said to start yielding when its von Mises stress reaches a critical value known as the yield strength, σ_y. The von Mises stress is used to predict yielding of materials under any loading condition from results of simple uniaxial tensile tests and it satisfies the property that two stress states with equal distortion energy have equal von Mises stress (Hibbeler, 2008; Gere, 2004).